Utrecht University

Masterthesis

Using X-ray spectroscopy to study the reduction and oxidation sensitivity of cobalt and nickel promoter species in conventional HDS catalysts

Author:
C.H.M. van Oversteeg

Supervisors:
M. al Samarai
Prof. Dr. F.M.F. de Groot

Inorganic Chemistry and Catalysis

Debye Institute for Nanomaterials

Department of Chemistry

February 9, 2015

Abstract

Hydrodesulfurization (HDS) is an important catalytic process in oil refining, in which sulfur is removed from organo sulfur compounds in crude oil. Conventional HDS catalysts consist of γ-alumina supported molybdenum sulfide slabs (MoS_2) promoted by either cobalt, nickel or both cobalt and nickel. Although the HDS catalysts are industrially used for a long time, the promoting effect of cobalt and nickel is still not fully understood. In this research X-ray absorption spectroscopy and microscopy were used to obtain deeper insight into the oxidation and reduction sensitivity of cobalt and nickel species present in promoted HDS catalysts. First, cobalt and nickel promoted MoS_2 catalysts were synthesized using incipient wetness impregnation methods. Samples were prepared by both simultaneous and sequential impregnation in order to study differences in morphology and activity between the impregnation methods. The impregnation was followed by a drying step, calcination procedure and sulfidation reaction to obtain the active sulfide catalysts. Although the catalyst samples were very sensitive to beam damage by an electron beam, STEM-EELS and TEM images showed that there was no difference in morphology between for samples promoted by different elements or samples prepared by different impregnation sequences. Furthermore, STEM-EELS and TEM showed the formation of typical MoS_2 slabs for all sulfide samples. Catalytic tests showed that all synthesized catalyst were active in thiophene desulfurization and verified the promoting effect by cobalt and nickel. However, a synergistic effect for double promotion could not be verified. An *in-situ* X-ray absorption experiment of an oxidation reaction was performed using a CoNiMoS sample and confirmed the oxidation of cobalt and nickel by analysis the Co- and Ni K-edges. CTM4XAS calculations indicated a transition from a Co 2+ T_d system to a mixture of Co 2+ O_h and Co 3+ O_h species. Furthermore an *in-situ* X-ray absorption experiment of a H_2 reduction reaction was performed using a CoNiMoO sample and confirmed the reduction of cobalt and nickel by analysis the Co- and Ni K-edges. CTM4XAS calculations were used to simulate the pre-edge structures of the Co K-edge and indicated a transition from a Co 2+ O_h system to a Co 2+ T_d system during the H_2 reduction reaction. From spectral elemental maps obtained from STXM measurements it was shown that molybdenum, cobalt and nickel are not homogeneously distributed on the aluminum support particle.

Table of Contents

1. Introduction

Crude oil is the most important natural resource for modern society. In 2013, about 90 billion barrels of oil were consumed world wide for their use as transportation fuels, lubricants and feed stocks for chemicals [1]. Crude oil consists of many different hydrocarbons, which differ in hydrogen-to-carbon atomic ratio, molar weight and boiling point. Many of the hydrocarbons present in crude oil contain unwanted heteroatoms such as sulfur (0-3%), nitrogen (0-0.5%), oxygen, vanadium and nickel [2]. The heavier hydrocarbons contain higher concentrations of these unwanted heteroatoms. Before the crude oil can be used, a complex refining process is used to lower the amount of unwanted heteroatoms and improve the product quality.
An undesirable heteratom debated extensively is sulfur. Fuel streams in refineries contain various organosulfur compounds, with thiophene and alkyl-substituted thiophenes, such as dibenzothiophene (DBT), as the most common [3]. The presence of sulfur compounds in fuels has multiple disadvantages. First of all, upon combustion sulfur compounds in fuels lead to the emission of sulfur oxide gases (SO_x). These gases form sulfates, which eventually leads to environmental concerns as acid rain, global warming and water pollution. As a consequence, strict environmental regulations in the United States and Europe state that the sulfur content in fuels must be lowered to below 0.1 ppm [4,5]. Secondly, the presence of sulfur has negative effects on the oil refining process. During the oil refining sulfur compounds cause corrosion in the refining equipment and tend to poison the catalysts. Thirdly, automotive catalytic converters are adversely affected by the presence of sulfur compounds in fuels. Due to the undesirable effects of sulfur compounds, hydrodesulfurization (HDS) is an important process in oil refineries. In this catalytic step sulfur is cleaved from hydrocarbons and H_2S is released [6]. Conventional catalytic HDS methods require severe operation conditions, such as high pressure and temperature. These conditions cause the hydrogenation of olefins, leading to excess hydrogen consumption and loss of octane rating. The H_2S formed in the HDS process is separated from the flue gas by amine scrubbing. Subsequently, the H_2S is partially oxidized to form elemental sulfur and water in the Clauss process [5,7,8].

Molybdenum or tungsten based catalysts are widely used for the removal of sulfur from organosulfur compounds. The most common catalyst for the HDS process is γ-alumina supported molybdenum disulfide (MoS_2). Alumina is extensively used as support material because of its outstanding mechanical and textural properties and relatively low costs [9,10]. To increase the catalytic activity this catalysts is promoted with either cobalt, nickel or both of them. Figure 1.1 shows the structure of molybdenum disulfide slabs as proposed by Topsøe et al. [11]. In these slabs molybdenum ions are sandwiched between two layers of sulfide ions. At room temperature the MoS_2 slabs contain some defects in the form of sulfur vacancies. The sulfur atom of a hydrocarbon can be inserted in these vacancies and subsequently the HDS reaction can take place.

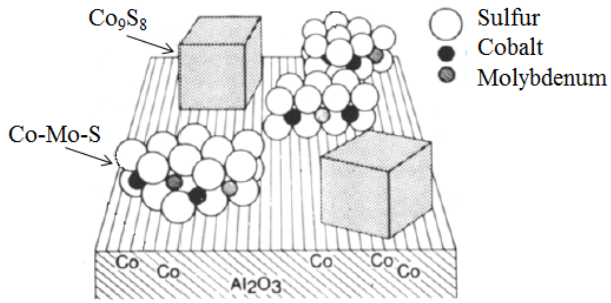

Figure 1.1: Schematic representation of a CoMoS catalyst used for the HDS process. The molybdenum disufide is ordered in slabs with the molybdenum ions sandwiched between the sulfide ions. Besides the active Co-Mo-S phase, inactive molybdenum and cobalt phases are present [11].

In this context some organic molecules as mercaptans (R-SH), sulfides (R-S-R) and disulfides (R-S-S-R) are relatively easy to desulfurize, whereas other molecules such as thiophenes and its derivatives require better catalysts to achieve high desulfurization rates. This can be explained by the structure of the molecule and steric effects around the sulfur atom [12]. Two suggested pathways for thiophene desulfurization are the hydrogenation pathway and the direct desulfurization pathway [13]. Figure 1.2 gives a schematic representation of the hydrogenation pathway mechanism for thiophene desulfurization. First the thiophene is hydrogenated in two steps. Next, the formed tetra hydro-thiophene adsorbs with its sulfur atom towards the molybdenum. Subsequently, the carbon-sulfur bonds are broken in two steps. Most likely this is done by two β -hydrogen eliminations. The formed butadiene desorbs into the gas phase and is further hydrogenated to 1-butene. Finally, the 1-butene is converted into the more thermodynamically stable cis and trans 2-butenes. The direct desulfurization pathway follows one hydrogen transfer, followed by a direct sulfur-carbon scission. In both mechanisms the active site is regenerated by the formation of H_2S.

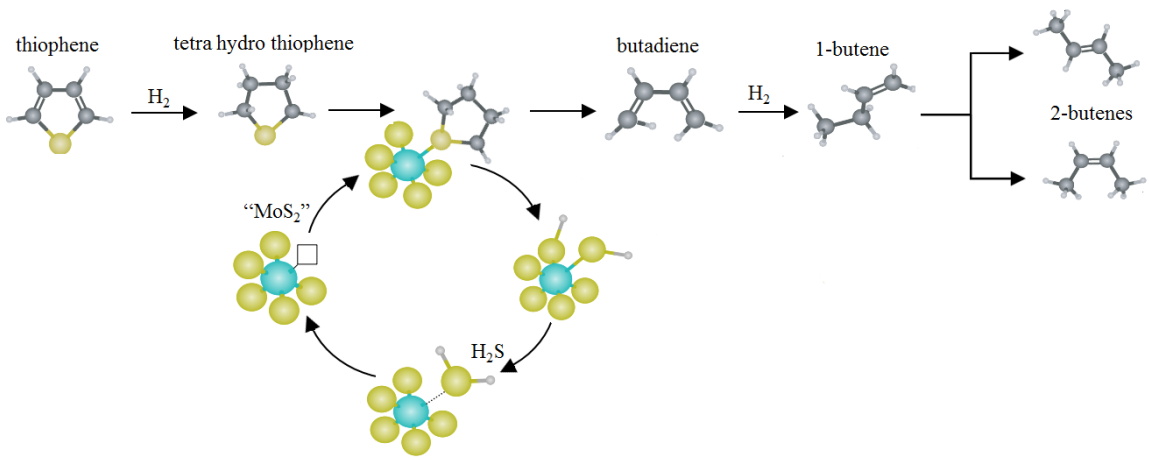

Figure 1.2: Schematic representation of the hydrogenation mechanism in the HDS of thiophene. The first step includes hydrogenation of the unsaturated ring, followed by adsorption on the catalyst. The C-S bonds are cleaved, resulting in butadiene. Subsequently, the butadiene is converted into the more thermodynamically stable cis and trans 2-butenes. Adapted from I. Chorkendorff et al. [2].

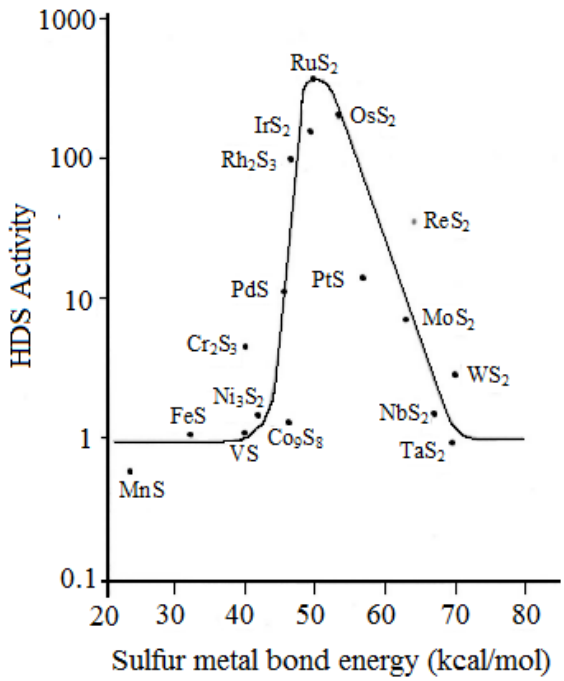

Figure 1.3: Volcano plot for the HDS activity of transition metals[2].

A sulfur vacancy in metal sulfides is assumed to be the active site of the HDS catalyst. Therefore, the bond strength between the sulfur atom and the catalyst is an important parameter for catalytic activity and obeys Sabatier's principle [14]. According to Sabatier's principle there is an optimal bond strength between the substrate and catalyst. At this bond strength the sulfur of the hydrocarbon can easily adsorb onto the catalyst, while the hetero atom can still be detached from the catalyst to regenerate the active site. If the bond between the metal and sulfur is too weak, the catalyst will have low affinity for the sulfur and sulfur adsorption will be the rate-limiting step. On the contrary, if the bond strength between the sulfur and metal is too high, only few sulfur vacancies will be present resulting in a low reaction rate. The volcano plot given in Figure 1.3 shows the metal sulfur bond strength versus the HDS activity. The highest activity is given for ruthenium, osmium, iridium and rhodium based catalysts, however due to their high price they are not suitable for practical use. Instead, MoS_2 and WS_2 catalyst are most often used in industry.

To increase activity, HDS catalysts are promoted by cobalt or nickel. Spectroscopic studies by Topsøe et al. revealed that the active cobalt or nickel species are located on the edges of the MoS_2 slabs (Figure 1.1) [15]. Besides the active promoters on the edges of the MoS_2 slabs, parasitic promoter phases are also present. For example, besides the Co-Mo-S phase, cobalt is also present as Co_9S_8 or as cobalt ion doped in the Al_2O_3 support. The exact role of the promoters is still not fully understood. The conversion rate for unpromoted MoS_2 catalysts is limited by slow active site regeneration and it is suggested that the cobalt and nickel atoms could facilitate the formation of sulfur vacancies. This is supported by recent studies by Moses et al. [16]. They conclude that, besides the bulk property metal-sulfur bond strength, surface properties, such as H-S binding energy, affect the HDS activity. Strong H-S binding energies will limit active site regeneration. By promoting the catalyst with cobalt or nickel, the H-S binding energy decreases and consequently the regeneration of the active site is no longer the rate limiting step.

The most common method to synthesize HDS catalysts is by incipient wetness impregnation. Following this procedure, metal precursors are dissolved in water and a specific volume

of this solution is added to a solid support material. The volume of the solution added is equal to the specific pore volume of the support material. This specific pore volume is determined by N_2 physisorption. The impregnated salt solution will be drawn into the pores by capillary forces. Subsequently, the impregnated support material is dried to dehydrate the metal salts, followed by a calcination step to decompose the precursor species and form the respective metal oxides. Conditions such as temperature, heating rate, gas flow and time have a large influence on the species formed and the distribution of the active components. The conventional cobalt and/or nickel promoted MoS_2 HDS catalysts can be prepared by various impregnation routes. The promoter(s) and molybdenum can be impregnated simultaneously or sequential. In the latter case, series of impregnation and drying/heat treatment steps result in a more time consuming and elaborate synthesis process. Furthermore, components impregnated in the first step can be redissolved and redistributed during the subsequent impregnation steps and the multiple drying and heat treatment steps may be unfavorable for catalyst quality. As a result co-impregnation is often more favored and is stated to have a higher HDS activity than sequential impregnation [17,18].

The catalyst oxides are not stable under HDS conditions and therefore the catalyst oxide precursors are sulfided to the active sulfide catalyst. During the so-called sulfidation reaction the oxide catalyst is brought in equilibrium with the HDS environment. The ideal active catalyst has a specific structure where sulfidic cobalt and nickel species decorate edges of molybdenumsulfide slabs. Therefore the sulfidation should be well-controlled rather than allowing the sulfidation to take place in the initial period of a HDS run [19]. As a consequence, the oxide catalyst is converted into the active sulfide catalyst in a presulfiding procedure prior to HDS reaction. During a gas-phase presulfidation a H_2S/H_2 gas mixture is flown through the oxide catalyst at elevated temperatures.

Besides their use as oxide precursor for HDS catalysts, cobalt and nickel promoted molybdenum oxides are used as catalysts for the partial oxidation of hydrocarbons [20–23]. As a consequence, a better understanding of the HDS catalysts and research on the oxide precursor for HDS catalysts can also help to investigate the partial oxidation catalysts. The partial oxidation process is used to produce H_2 and synthesis gas by the reaction of hydrocarbons with O_2 involving an exothermic process. The produced H_2 can be used as efficient fuel, since exhaust emissions of hydrocarbons and CO are lower compared to the use of conventional fuels. The production of synthesis gas, a mixture of H_2 and CO, is of interest since it is used in synthetic fuel production and methanol synthesis.

HDS catalysts are industrially used for decades. However, their catalytic activity and the promoting effects of cobalt and nickel are still not fully understood. A better understanding of the behavior of the different elements present in the catalyst is helpful in further improving the catalyst performance. The aim of this research is to get deeper insight in the behavior of cobalt and/or nickel promoted catalysts during oxidation and reduction reactions. Catalysts promoted by either cobalt, nickel or both cobalt and nickel were synthesized by simultaneous and sequential impregnation methods. The influence of the different impregnation methods and promoter species on the morphology and activity of the catalysts was investigated using X-ray diffraction, electron microscopy and catalytic tests. The reduction and oxidation behavior of cobalt and nickel species was studied using *in-situ* X-ray absorption experiments. A better understanding of the behavior of the catalyst under reduction and oxidation conditions can contribute towards a better understanding of the behavior of the different elements present in the catalyst.

2. Theory

2.1 Standard catalyst characterization techniques

2.1.1 N_2-physisorption

N_2-physisorption is a technique that is used to obtain information about morphological details of porous materials [24]. In this research the technique is used to determine the pore volume of the support material. The technique is based on equilibrium conditions and the physisorption of N_2-gas on the surface of a porous material. A typical physisorption set-up is depicted in Figure 2.1. Two known volumes V_1 and V_2 are connected with a valve in between. The porous sample is located in V_2, while the pressure is measured only in V_1. Both the volumes can be filled and evacuated separately through valve 1 and valve 2 respectively. During the measurement, gas pressure is increased in multiple steps from p=0 to the condensation pressure p_0 and then decreased back to p=0. In each step, the pressure is varied in V_1 while valve 3 is closed. Subsequently, valve 3 is opened to equalize the pressure in both volumes. As some of the gas is adsorbed on the sample, the pressure will be lower once the equilibrium is reached. During this pressure variation the extra amount of gas needed to reach equilibrium is measured. By plotting the volume versus the p/p_0 an adsorption isotherm is obtained. Such an isotherm is schematically depicted in Figure 2.1. Due to capillary forces, the pores are completely filled at a pressure lower than the condensation pressure p_0, causing a sudden jump in the isotherm. At lower pressures the smaller pores are filled, whereas larger pores are filled at higher pressures. The pore radius is calculated by the Kelvin equation (Equation 2.1), which relates the partial pressure to the pore radius.

$$\ln \frac{p}{p_0} = \frac{2\gamma V_m}{rRT} \tag{2.1}$$

In this equation, p is the partial pressure, p_0 is the condensation pressure, γ is the surface tension, V_m is the molar volume, r is the effective radius of the droplet and thus the pore, R is the gas constant and T is the temperature.

The slope of the red part of the isotherm gives an indication about the pore size distribution. Since the pore size determines the pressure at which the pore is filled, pores with different sizes will fill at different pressures. Consequently a large pore size distribution results in a more gradual capillary filling, hence a less steep slope.

2.1.2 X-ray Diffraction

In this research X-ray Diffraction was used as qualitative analysis method to identify the crystalline phases present in the samples [25]. During an experiment the sample is irradiated with a monochromatic X-ray beam. When the X-rays interact with atoms in a periodically ordered lattice they are diffracted in a specific angle. If the diffracted X-rays are in phase they will show constructive interference. In a diffractogram the intensity of the scattered X-rays is plotted versus the angle 2θ between the incoming and diffracted beam. Peaks in the diffractogram will correspond to a scattering angle where constructive interference occurs. Bragg's law relates the diffraction angle at a certain point to the lattice spacing (Figure 2.2). Since the lattice spacing is characteristic for a material, the angle of diffraction gives information about the crystalline phases present.

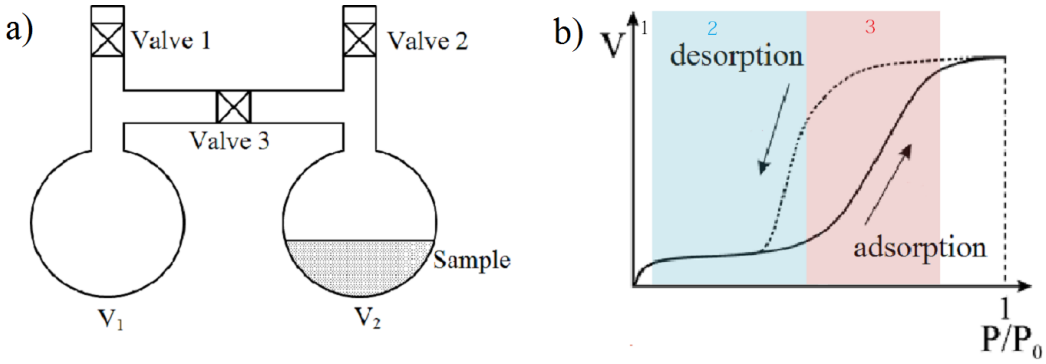

Figure 2.1: Physisorption: a) Schematic representation of a physisorption set-up. b) Example of a physisorption isotherm. During the N_2 adsorption measurement, pressure is increased. 1: Micropores are filled. 2: A layer of nitrogen is formed on the surface of the material. 3: Mesopores are filled at the highest pressures.

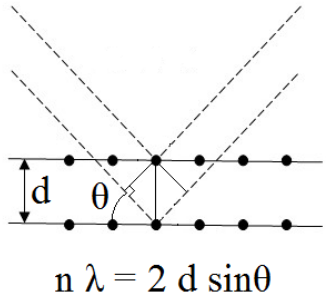

Figure 2.2: X-rays scatter constructively in directions given by Braggs law [25].

2.1.3 Transmission Electron Microscopy

Transmission Electron Microscopy (TEM) is a microscopy technique that can be used to determine shape and size of particles [26]. This technique is similar to visible light microscopy (VLM). However, where VLM uses visible light as light source, in TEM electrons are used. In VLM, the lateral spatial resolution of the microscope is limited by the wavelength of a photon as dictated by Equation 2.2, an adapted form of Abbe's diffraction limit.

$$d = constant \cdot \frac{\lambda}{n \cdot sin\theta} \tag{2.2}$$

From this equation is can be seen that a decrease in the wavelength improves the lateral spatial resolution. Since the wavelength of electrons is related to their energy via the Broglie equation (Equation 2.3), electrons have very small wavelengths. Consequently, the resolution of TEM is much higher than for VLM. With TEM it is possible to view objects with sizes in the order of a few Ångström.

$$\lambda = \frac{1.22}{E^{0.5}} \tag{2.3}$$

During a TEM measurement electrons are generated by a current flowing through a thin tungsten thread. This results in the emission of electrons. The microscope is kept under high vacuum. The electrons moving through the microscope are focused by a pinhole and several electromagnetic lenses. Eventually they collide with the sample. As can be seen in Figure 2.3, several interactions are possible for the electrons with the sample. Part of the electrons pass through the sample without losing their energy. As the attenuation of the electrons is

dependent on sample thickness and density, the transmitted electrons are used to create a TEM image. Darker areas in the image represent more dense parts of the sample, since less electrons are transmitted through thicker areas. To obtain statistically representative results, various locations of the samples are imaged.

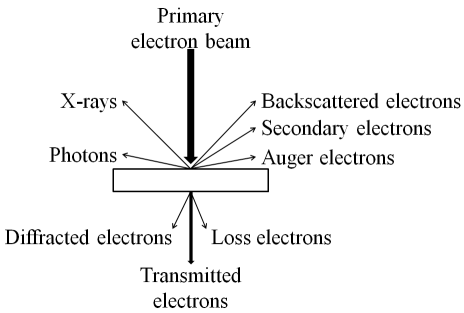

Figure 2.3: Several detectable signals are possible when the electron beam interacts with the sample. TEM detects electrons transmitted through the sample [26].

2.1.4 Energy Dispersive X-ray Spectroscopy

Energy Dispersive X-ray Spectroscopy (EDX) in combination with TEM is a technique that is used for local element analysis [27]. During an EDX measurement, electrons are collided with the sample. These collisions give rise to several phenomena, including the emission of X-rays, used in EDX spectroscopy (Figure 2.3). Figure 2.4 shows a schematic overview of the X-ray fluorescence phenomena that can occur when electrons from the incoming electron beam interact with atoms at the surface of the sample. During this process, a bound electron from an atomic orbital is excited to the continuum, resulting in a core hole. When the core hole is filled with an electron from a higher atomic orbital, X-ray fluorescence occurs. The energy of the emitted X-ray corresponds to the energy difference between the two atomic orbitals and is characteristic for the emitting atom. By fixing the electron beam on specific positions, local composition of a sample can be determined. Furthermore, by comparing the intensities of different elements, relative elemental compositions can be found.

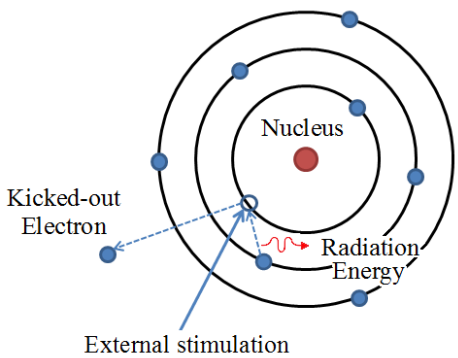

Figure 2.4: During the EDX process, an incident electron interacts with a bound electron from a surface atom. The bound electron is ejected, resulting in a core hole. This core hole is then filled by the decay of an electron from a higher atomic orbital, resulting in X-ray fluorescence [27].

2.2 Core level spectroscopy and microscopy

Core level spectroscopy provides both structural and electronic information about materials [28]. Core electrons are the electrons bound in the deepest orbitals and unlike valence electrons, they are almost unaffected when the atom is condensed into a solid. Most of the properties of solids are thus determined by the valence electron states. In core level spectroscopy these valence electron states are studied by the excitation of core electrons to the empty density of states. To cause transitions from core to valence states X-ray photons are used as they have the required energy for these transitions. The excitation of a core electron by the absorption of X-ray radiation results in a core hole. The core hole can be filled up by the decay of an electron from higher orbitals in an X-ray emission process. If the electron decays from a different state than that of final state of the excitation, the emission is called inelastic ($\Delta E \neq 0$). The X-ray emission is elastic if the electron decays from the same state as the final state of the excited electron ($\Delta E = 0$). Figure 2.5 gives an overview these absorption and emission processes. The core hole will have a certain life time before an electron decays to the ground energy state [29]. As given by the Heisenberg uncertainty relation, the life time of a core-hole τ results in an uncertainty in the energy Γ and therefore broadening in the absorption spectrum as given in Equation 2.4.

$$\Gamma\tau \cong \hbar = 10^{-16} \text{ eV s} \tag{2.4}$$

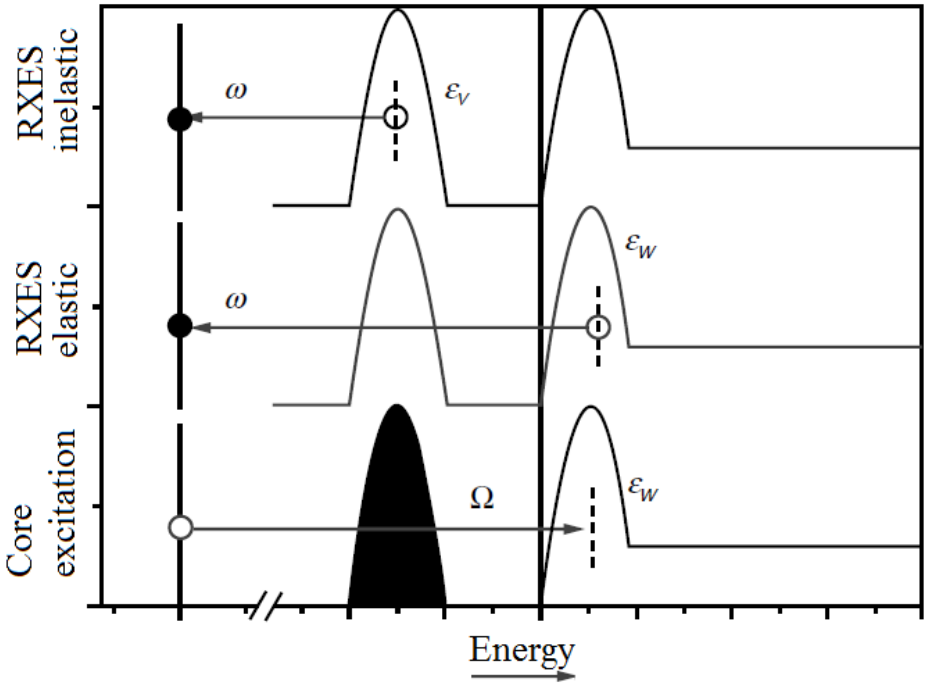

Figure 2.5: The excitation of a core electron is given in the bottom frame. The two top frames give the elastic and in-elastic RXES processes in which the core hole is filled by the decay of the excited electron or another energy level, respectively. Adapted from de Groot et al. [29].

Most core level experiments require a scanable energy and high flux. Consequently core level spectroscopy is performed at synchrotron radiation facilities [30]. In a synchrotron electrons are generated by an electron gun. Next, the electrons are accelerated in a linear accelerator and booster ring using radio frequency waves. By acceleration the kinetic energy

of the electrons is increased. When electrons reach certain speed they are injected into the storage ring, which contains several insertion devices. As the electrons pass through the insertion devices the beam is forced to perform undulations or wiggles. In this way the emission of highly brilliant, forward-directed radiation is stimulated. The obtained photon beam, with various energies depending on the angle of curvature, is directed to a beamline endstation where the desired wavelength can be chosen out of a continuous spectrum from infrared to hard X-ray radiation.

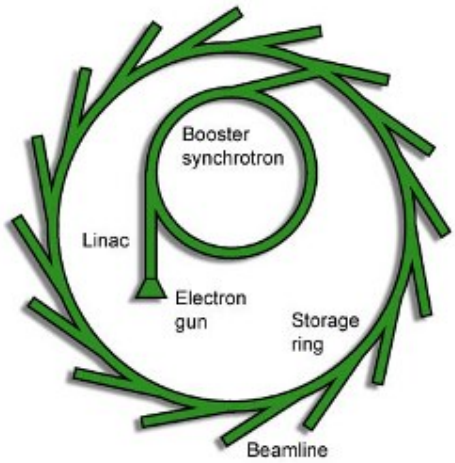

Figure 2.6: Schematic representation of a synchrotron [31]. Electrons are generated by an electron gun. Subsequently the electron beam is directed to the linear accelerator, booster ring, storage ring and finally directed to the beamline endstation.

An important rule in the interaction of X-rays with matter is the Fermi Golden Rule (Equation 2.5) [29,32]. This rule gives the transition probability (W) between the initial (ϕ_i) and final state (ϕ_f). A transition can take place if the energy of the X-ray photons is equal to the energy difference between the initial and final states. Conservation of energy is included by the delta function, with E_f the final state energy, E_i the initial state energy and $\hbar\omega$ the energy of the incident photon. The delta function implies a sharp absorption line at certain energy. However, due to the life time broadening (Γ) discussed before, the observed peaks are broadened. The transition operator T is related to the interaction Hamiltonian (H_{INT}) as given by Equation 2.6. In this equation H gives the Hamiltonian of the unperturbed system.

$$W_{fi} = \frac{2\pi}{\hbar}|\langle\phi_f|T|\phi_i\rangle|^2\delta_{E_f-E_i-\hbar\omega} \tag{2.5}$$

$$T = H_{INT} + H_{INT}\frac{1}{E_i - Hi\Gamma/2}T \tag{2.6}$$

X-ray absorption is a one-photon process. This process can be described by a first-order perturbation of the interaction Hamiltonian, giving the transition operator T_1. By insertion of the vector potential and by rewriting the equation using the first two terms of the Taylor expansion of $e^{ikr} = 1 + ikr + ...$, the transition operator T_1 is given by equation 2.7. The electric dipole transition is represented by the first term in brackets $e_{k\lambda} \cdot p$ and the electric quadrupole transition is represented by the second term $i(e_{k\lambda} \cdot p)(k \cdot r)$

$$T_1 = \sum_{k\lambda} b_{k\lambda}\frac{e}{mc}A_0[(e_{k\lambda}\cdot p) + i(e_{k\lambda}\cdot p)(k\cdot r)] \tag{2.7}$$

The wavelength of the X-ray photon is much larger than the typical size of an atom. Therefore, the factor kr is much smaller than 1 ($kr \ll 1$). Consequently, the quadrupole term in the transition operator is much smaller and quadrupole transitions can most often be neglected. In this case the dipole approximation can be used. The transition operator then turns into the dipole operator r. As a result the Fermi Golden rule can be rewritten as :

$$\mathrm{W}_{fi} \propto |\langle \phi_f | r | \phi_i \rangle|^2 \delta_{E_f - E_i - \hbar\omega} \tag{2.8}$$

For excitations from the 1s core states (K-edges) the interactions between electrons in the final state are relatively weak. As a consequence X-ray absorption can be described by a single electron excitation approximation. In this case the initial state can be written as a core wave function (ϵ) and the final state wavefunction as a valence electron wavefunction (ν)(Equation 2.9). The squared matrix element M can be assumed as a constant as it only has a small variation in energy. The delta function in the Fermi Golden rule suggests that we can obtain the density of states. Subsequently the Fermi Golden rule can be rewritten as Equation 2.10.

$$|\langle \phi_f | r | \phi_i \rangle|^2 = |\langle \epsilon | r | \nu \rangle|^2 = M^2 \tag{2.9}$$

$$I_{XAS} \sim M^2 \rho \tag{2.10}$$

If the interactions between electrons in the final state cannot be neglected, the single electron excitation approximation is no longer valid. This is the case for the 3d transition metal L-edges where an electron is excited from a 2p to a partly filled 3d shell. The 2p core state and 3d valence state have a large overlap and their interaction cannot be neglected. In this case the initial state is a $3d^n$ wavefunction and the final state a $2p^5 3d^{n+1}$ wavefunction. The electric dipole operator can then be written as given in Equation 2.11.

$$|\langle \phi_f | r | \phi_i \rangle|^2 = |\langle 2p^5 3d^{n+1} | r | 3d^n \rangle|^2 \tag{2.11}$$

Due to the overlap between the core and valence states the spin-moment of the core hole interacts with the valence electrons and gives rise to an exchange splitting. If the core hole also carries an orbital momentum, the spin-orbit coupling separates the 2p levels into $2p_{3/2}$ and $2p_{1/2}$, referred to as L_3 and L_2 edge, respectively. These effects caused by the overlap between core and final states are called multiplet effects. The multiplet effects will modify the spectral shape and the number of observed peaks. As a consequence the absorption spectrum will no longer represent the density of states.

In order for a transition to be allowed two selection rules should be obeyed. Since the orbital momentum of a photon is one, interaction of a photon with the material can only change the orbital quantum number of the material by one. This leads to the first selection rule, which states that the orbital quantum number of the final state can only differ by one from the initial state (Δ L = +1 or -1). According to this selection rule a transition from an s orbital will be into a p orbital, i.e. from l=0 to l=1. The main quantum number does not have a selection rule. Therefore both 1s2p and 2s2p transitions are allowed. A second selection rule is the spin selection rule. As light does not carry spin the spin of an electron can not be modified during an interaction with light (Δ S = 0). If both these selection rules are obeyed the dipole matrix element is non zero and a transition is fully allowed. Fully or partly forbidden transitions can sometimes be observed as weak bands in an absorption spectrum. This is caused by hybridization of orbitals, which relaxes the selection rules.

In the presence of spin-orbit coupling, the orbital angular momentum L and spin angular momentum S are no longer good quantum numbers. The only valid quantum number in this case is the total angular momentum quantum number J. An example in which spin-orbit

coupling is important are the transition metal L-edges, where the p core states are dominated by a large core hole spin-orbit coupling. In the presence of spin-orbit coupling, the selection rules mentioned above are no longer valid and the new selection rule states that the total quantum number J can change by minus one, zero and one (Δ J = -1, 0, 1). In addition, the value of the final state cannot be equal to zero if the J value of initial state is zero (J=J'$\neq$0).

2.2.1 X-ray Absorption Spectroscopy

If X-ray photons carry enough energy they are able to excite core electrons to empty density states of the material. In an X-ray absorption spectrum, energy is plotted against intensity. The X-ray absorption spectrum can be roughly divided into two regions, the X-ray Absorption Near Edge Structure (XANES) and the Extended X-ray Absorption Fine Structure (EXAFS) (Figure 2.7) [33,34]. The XANES region includes the absorption edge, the most characteristic spectral feature. At this edge a drastic increase in the absorption indicates that the incoming photon carries enough energy for the excitation of a core electron to the empty density of states. The energy of this absorption edge then corresponds to the binding energy of the electron in the K, L, M, etc, shells. The region before the edge is called the pre-edge. The features in this region are caused by partially forbidden quadrupole transitions. For example, for a 3d transition metal, the pre-edge region for the K-edge covers transitions from the 1s to 3d states. The spectral shape in the XANES region is determined by electronic density of states effects [35]. As a result the XANES region is strongly sensitive to the ligands surrounding the absorbing atom. It provides information about electronic properties (e.g. oxidation state) and the local geometry of the absorbing atom. The region above the edge is called the Extended X-ray Absorption Fine Structure (EXAFS), and is dominated by single scattering events of the outgoing electron on neighboring atoms [35]. Consequently the region gives information about the local atomic structure around the absorbing site.

For 3d transition metals, the K-edge is found in the hard X-ray regime (5-10 keV). The edge corresponds to transitions from the 1s to 4p states, while the corresponding pre-edge covers transitions from the 1s to 3d states. L-edges for 3d transition metals are found in the soft X-ray regime (400-1000 eV) and correspond to transitions from the 2s and 2p states to the empty density of states [36]. Table 2.1 gives the nomenclature and binding energies of the elements involved in this research. As the K-edges are found in the hard X-ray regime, the experiments do not require high vacuum and can be measured under ambient conditions using a relatively low radiation dose. This gives the K-edges a big advantage over the soft X-ray L-edges, especially regarding *in-situ* experiments. However, as the life time of the 1s core hole is short, the life time broadening is high (1-2 eV) and about three times broader than the broadening found for corresponding L-edges. Due to this large life time broadening the K-edges are less defined and are harder to analyze and simulate, when compared to the corresponding L-edges.

Table 2.1: Nomenclature and binding energies (in eV) for molybdenum, cobalt, nickel and alumina [37].

Orbital	Label	E(Mo)	E(Co)	E(Ni)	E(Al)
1s	K	20000	7709	8333	1559.6
2s	L_1	2866	925.1	1008.6	117.8
$2p_{\frac{1}{2}}$	L_2	2625	793.2	870.0	72.95
$2p_{\frac{3}{2}}$	L_3	2520	778.1	852.7	72.55

In the 3d metals, often used for catalysis, information about the partially filled 3d states is crucial to understand the catalysis caused by the element. The 3d states can be directly

probed by measuring 2p→3d transitions ($L_{2,3}$ edges). Using the dipole approximation, K-edges will give information about the empty metal 4p-states, while the pre-edge structure gives information about the 3d states.

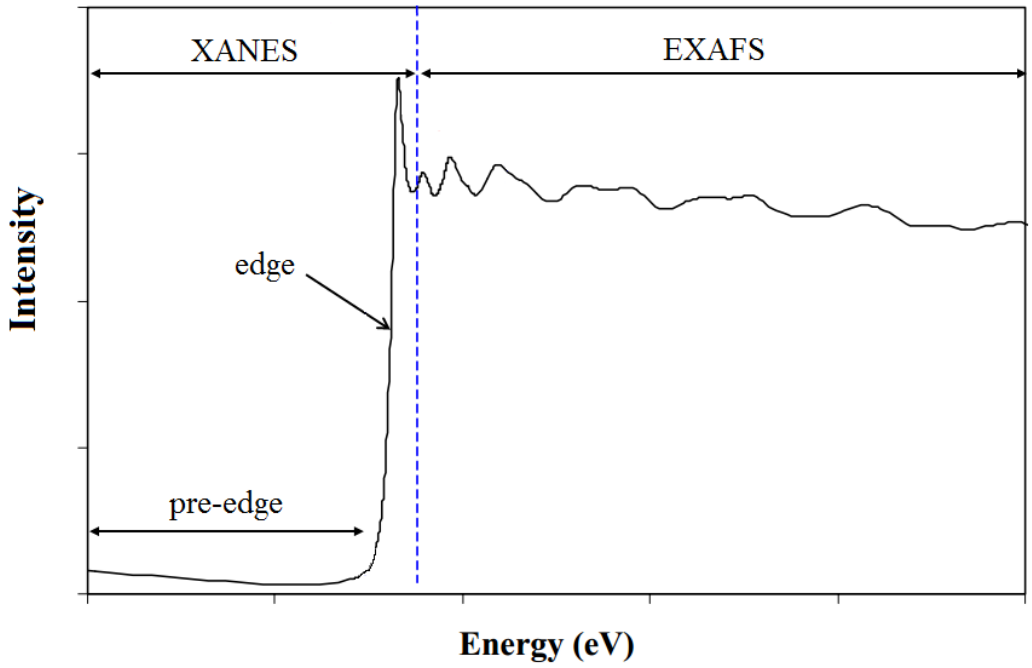

Figure 2.7: Example of a typical X-ray absorption spectrum. The XANES region gives information about electronic properties and local geometry, whereas the EXAFS region provides information about the local atomic structure around the absorbing site. Adapted from Paul Scherrer Institut [38].

2.2.2 Scanning Transmission X-ray Microscopy

Scanning transmission x-ray microscopy (STXM) is a technique that combines XAS and microscopy. The specimen is raster scanned in x,y direction by a X-ray beam, while the transmitted or emitted photons are monitored in the transmission or fluorescence mode, respectively. As discussed before, the lateral spatial resolution of a microscope is limited by the wavelength. Therefore, the resolution of X-ray microscopy lies in between that of a visible light microscope and an electron microscope. Because the interaction of X-rays is much less with matter compared to electrons, the sample is less sensitive to radiation damage and the penetration depth of X-rays is much larger compared to electrons. This gives X-ray microscopy the ability to analyze thicker samples. Consequently X-ray microscopy gives a unique combination between resolution and penetration depth.
Figure 2.8 gives a schematic representation of a STXM set-up. First, a zone plate (ZP) is used to focus X-rays to the sample using diffraction. The diffracted light interferes constructively at the focal spot, where the image is created. To filter out the first order light needed for the STXM experiment, an order sorting aperture (OSA) is placed between the zone plate and specimen. During an experiment the sample is raster scanned and transmitted or emitted x-rays are detected by a CCD camera.

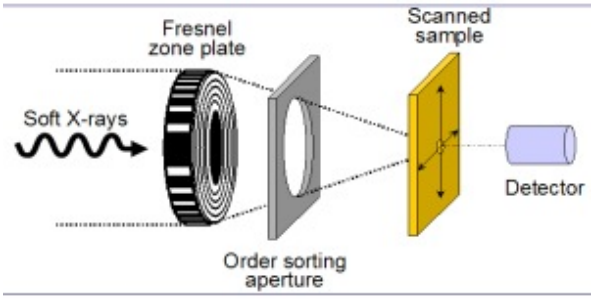

Figure 2.8: Typical layout of a STXM chamber [39]. The sample is placed in mechanical stage. The X-rays are focused and optimized by the zone plate (ZP) and order sorting aperture (OSA). Part of the X-rays will be transmitted by the sample and will be detected by a CCD camera.

Absorption spectra are measured at every spot of the image. In this way spectromicroscopy can be used to obtain local chemical information about the sample, such as oxidation state and coordination around the element. The lateral resolution for this technique is currently around 20 nm [40].

2.2.3 Scaning Transmission Electron Microscopy - Electron Energy Loss Spectroscopy

The electron-analog of STXM is Scanning Transmission Electron Microscopy- Electron Energy Loss Spectroscopy (STEM-EELS). STEM-EELS is a powerful tool for element analysis. EELS is based on the energy loss of electrons caused by inelastic scattering events[40]. Inelastic scattering involves the interaction between incident electrons with bound electrons. Energy exchange between the incoming and atomic electrons is possible. By measuring the energy loss of the electrons and plotting this versus the electron count, information about the interactions of the electrons with the sample can be obtained. At high scattering energies inner-shell excitations can be observed corresponding to the binding energies of the inner atomic shells [41]. Consequently, the energy-loss spectrum can be used for elemental analysis. EELS combined with STEM is capable of obtaining very high spatial resolution as the electron beam can be focused in to a 'probe' with an extremely small diameter. In the most ideal case STEM-EELS combines atomic spatial resolution with single atom compositional sensitivity [42]. However, this technique operates under high vacuum conditions, which makes the technique unsuitable for performing *in-situ* experiments.

3. Experimental methods

3.1 Catalyst synthesis

3.1.1 N_2-physisorption

The pore volume of the support material γ-alumina was determined by N_2 physisorption. Nitrogen adsorption and desorption isotherms were measured at 77 K on a Micromeritics TriStar 3000 device. About 0.1 gram of γ-alumina was used for the measurement.

3.1.2 Incipient wetness impregnation

Catalysts were synthesized by incipient wetness impregnation on a γ-alumina support (BASF Al-4184, surface area 250 m^2/g, pore volume 0.70 mL/g). Before impregnation, the support was dried under vacuum for 16 hours to remove water and air from the porous material. For each synthesis 2 gram of γ-alumina was used. Aqueous solutions of ammonium heptamolybdate hexahydrate (AHM, $(NH_4)_6Mo_7O_{24} \cdot 6\ H_2O$, Sigma Aldrich, 99.98% trace metals basis), cobalt nitrate hexahydrate ($Co(NO_3)_2 \cdot 6\ H_2O$, Acros Organics, 99+%) and nickel nitrate hexahydrate ($Ni(NO_3)_2 \cdot 6\ H_2O$, Sigma-Aldrich, 99.999% trace metals basis) were used. Weight loadings of 14 wt% for molybdenum and 5 wt% for both cobalt and nickel were aimed. Then, the impregnated support was kept at vacuum for 30 minutes. Subsequently the powder was transferred to a top-down reactor for drying and heat treatment. All drying and heat treatment steps were performed under 75%N_2/O_2 flow with a flow rate of 1 mL/min. First, the sample was dried at 60 °C for 16 hours, followed by drying at 120 °C for 1 hour to remove all water and dehydrate the metal salts. To convert the impregnated precursors of molybdenum, cobalt and nickel to their respective metal oxides, the sample was calcined at 450 °C for 16 hours.

3.1.3 Sulfidation procedure

The metal oxides were converted into metal sulfides in a sulfidation procedure. A metal oxide sample was transferred to a top-down reactor. This reactor was flushed with helium for 20 minutes to remove air from the reactor. Subsequently the sample was heated to 450 °C with a ramp of 10 °C /min while flowing a 10% H_2S/H_2 mixture through the reactor (1 mL/min). The sample was kept at 450 °C for 5 hours after which the H_2S/H_2 flow and heating were stopped. At 200 °C the reactor was flushed with helium to remove remaining H_2S/H_2. After cooling down to room temperature, the sulfided samples were stored in a N_2 glovebox to prevent oxidation.
Table 3.1 gives an overview of all samples and corresponding synthesis method.

Table 3.1: Overview of sample names and corresponding impregnation methods.

Oxide catalyst precursor	Sulfide catalyst	Impregnation method
MoO1	MoS1	single impregnation
CoMoO1-sim	CoMoS1-sim	simultaneous impregnation
CoMoO2-seq	CoMoS2-seq	sequential impregnation
CoMoO3-seq	CoMoS3-seq	sequential impregnation
CoMoO4-sim	CoMoS4-sim	simultaneous impregnation
NiMoO1-sim	NiMoS1-sim	simultaneous impregnation
NiMoO2-seq	NiMoS2-seq	sequential impregnation
CoNiMoO1-sim	CoNiMoS1-sim	simlutaneous impregnation
CoNiMoO2-seq	CoNiMoS2-seq	sequential impregnation
CoNiMoO3-sim	CoNiMoS3-sim	simultaneous impregnation

3.2 Standard catalyst characterization techniques

3.2.1 X-ray Diffraction

The crystalline phases of the oxidic precursors were identified by X-ray diffraction (XRD). Samples were loaded into a flat sample holder and introduced in a Bruker-Nonius D2 Advance X-ray diffractometer set-up. Co-Kα radiation with a wavelength of 1.79026 Å was used. Spectra were measured with a 2θ range from 10 ° to 80 ° using an increment of 0.1 ° and steptime of 1s. All measurements were performed at room temperature.

3.2.2 Transmission Electron Microscopy and Energy Dispersive X-ray Spectroscopy

Transmission electron microscopy and energy dispersive X-ray spectroscopy were carried out using a Technai 20 FG electron microscope using an accelerating voltage of 200kV. The oxide catalysts samples were suspended in ethanol using an ultrasonic bath. The samples were disposed onto a polymer grid with carbon and air-dried. Sample preparation for the sulfide catalysts was done in a glovebox filled with N_2 to avoid contact with air. The sulfide samples were suspended in methanol, followed by disposal on the polymer grid and air drying. Sulfide samples were exposed to air for a few tens of seconds during introduction in the microscope chamber. Due to the apparent sensitivity of the oxide and sulfide samples towards beam damage, a so-called low dose mode was used.

3.3 Catalysis

Catalytic tests of sulfide catalyst samples were performed at Albemarle Catalyst B.V.. Here the activity of the catalyst samples in thiophene desulfurization was tested. Approximately 20 mg of each sulfide catalyst sample was used for the measurement. When introduced into the set-up, the sulfide catalysts were exposed to air for a short time. Therefore a short drying and sulfidation procedure was performed prior to the catalytic test to reduce the effects of oxidation. Drying was done at 120 °C under helium flow, followed by a temperature programmed sulfidation step at 320 °C under $H_2S/H_2/He$ flow. Prior to the catalytic test, the set-up was flushed using a H_2 flow at 320 °C. Subsequently, a 0.1μL pulse of thiophene was injected through the set-up. A flame ionization detector (FID) and a mass spectrometer (MS) were used to measure the initial activity after this first pulse. Afterwards, ten pulses of 1μL thiophene were injected, followed by another three pulses of 0.1μL thiophene. After

each of the last three pulses, the catalyst activity after stabilization was measured using FID and MS. The catalytic testing procedure is schematically depicted in Figure 3.1.

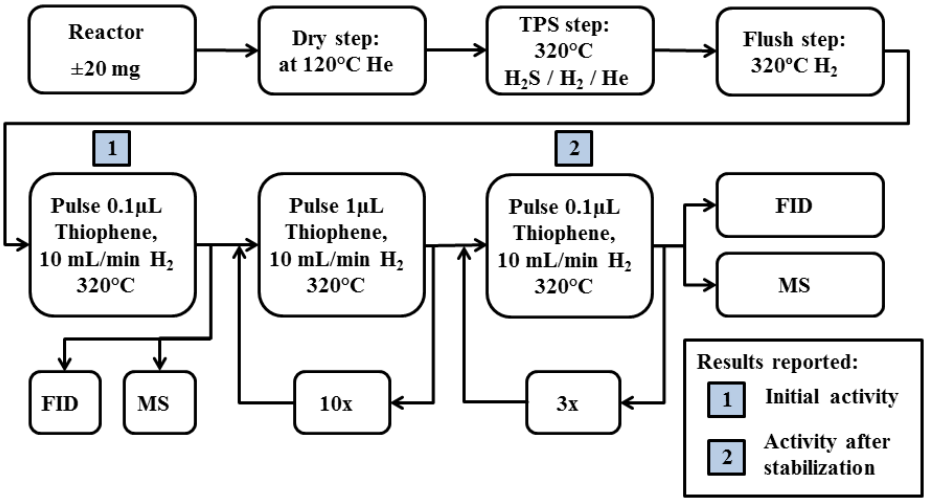

Figure 3.1: Schematic representation of the catalytic test performed at Albemarle Catalysts B.V.. Prior to the catalytic test, a short drying and sulfidation step were carried out. Thiophene conversion was measured at several stages of the thiophene HDS by FID and MS.

3.4 Core level spectroscopy and microscopy

3.4.1 Sensitivity of cobalt and nickel towards oxidation

The sensitivity of cobalt and nickel species towards oxidation was measured using *in-situ* X-ray absorption experiments. XAS experiments were performed at the Spring-8 synchrotron radiation facility in Japan. The sulfided catalyst CoNiMoS-3-sim was used for this *in-situ* experiment. Prior to the experiment a pallet of CoNiMo sulfide was pressed and placed into the sample holder, which contains a heating stage (Figure 3.2a). The pallet-holder was then placed inside the reactor (Figure 3.2b) which was mounted on the beamline set-up. The sample preparation and sealing of the reactor were done inside a glovebox to prevent oxidation of the sulfide sample. X-ray absorption was measured in the fluorescence mode.

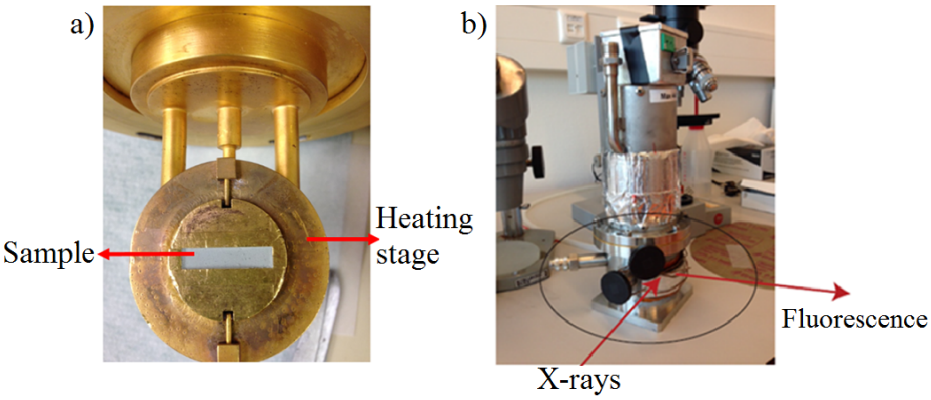

Figure 3.2: Pallet holder, heating stage (a) and reactor (b) used for *in-situ* XAS experiments.

In the first step, the cobalt and nickel K-edges were measured at room temperature under

argon atmosphere. Then, a quick non-resonant emission scan was done to determine the peak position of the K-edge. The cobalt non-resonant XES spectrum was obtained by exciting the sample at 7800 eV. Next, two XAS spectra were recorded with an energy range of 7705-7740 eV. The same sequence of XES and XAS (2x) measurements was repeated for the Ni K-edge. The nickel non-resonant XES spectrum was measured by excitation at 8500 eV. For the nickel absorption spectra an energy range of 8330-8375 eV was used.
To perform *in-situ* experiments, the catalyst sample was heated to several temperatures (50 °C, 80 °C, 120 °C, 200 °C and 400 °C), while flowing air through the reactor. The sample was left at the elevated temperature for 1 hour. Finally the sample was cooled down to room temperature before each of the consecutive measurements. When the sample reached room temperature the non-resonant XES and XAS (2x) measurements at the cobalt K-edge were started. For nickel only the first two steps of the *in-situ* oxidation reaction were measured. A schematic representation of the *in-situ* experiment is shown in Figure 3.4.

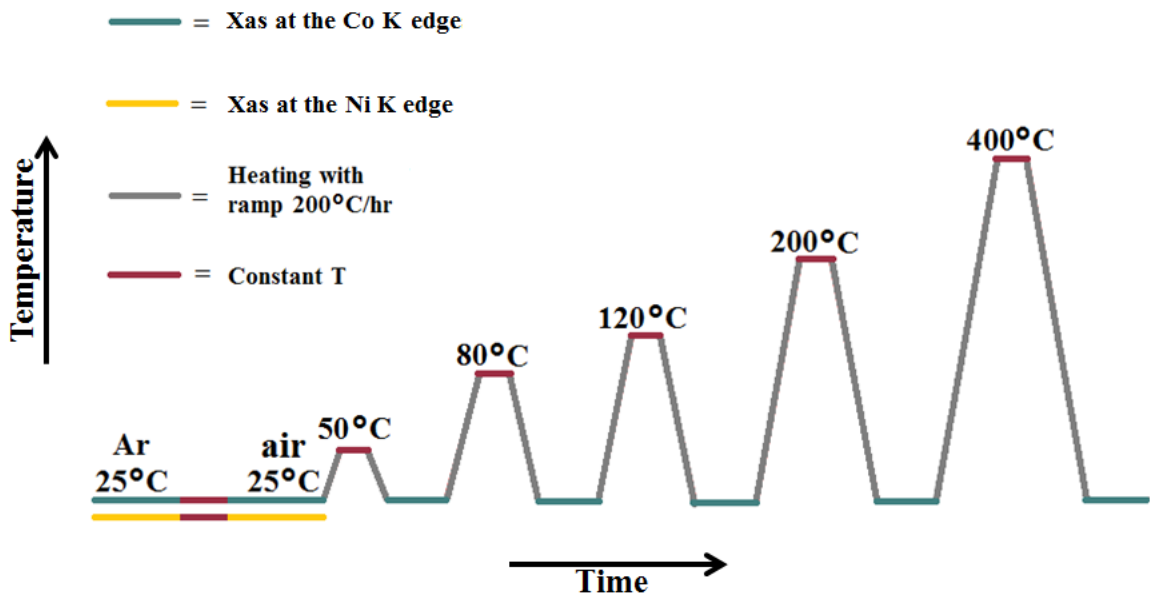

Figure 3.3: Overview of the *in-situ* XAS oxidation experiment. To perform *in-situ* experiments the reactor catalyst sample was heated to several temperatures while flowing air through the reactor. The sample was kept at this temperature for 1 hour for every consecutive temperature step. XAS measurements were performed when the sample was cooled down to room temperature. For nickel only the first two steps of the oxidation were measured.

The software CTM4XAS was used to simulate the K pre-edge region of cobalt in order to elucidate the trends seen in this region of the absorption spectra [43]. Parameters used for the calculations are given in Table 3.2.

Table 3.2: Overview parameters used for calculation of the Co pre-edge region using CTM4XAS.

Ion	Symmetry	10 dq
Co2+	Td	-0.6 eV
Co2+	Oh	1 eV
Co3+	Oh	2.3 eV

3.4.2 Sensitivity of cobalt and nickel towards H_2 reduction

The sensitivity of cobalt and nickel towards H_2 reduction was measured using *in-situ* X-ray absorption experiments. XAS experiments were done at the Stanford Synchotron Radiation Lightsource (SSRL) at beamline 6-2b. By the absorption of X-ray photons the K-edges of both cobalt and nickel of the catalyst oxide CoNiMoO-sim-3 were studied. Prior to the experiment a pallet of CoNiMo oxide was pressed and placed into the sample holder. The same reactor as used for the oxidation experiment was used (Figure 3.2). X-ray absorption was measured in the fluorescence mode.

In the first stage, the cobalt and nickel K-edges were measured at room temperature. A quick non-resonant emission scan was performed to determine the peak position of the K-edge by fluorescence. For cobalt the monoexcitation for the non-resonant XES spectrum was set at 7800 eV. The spectrum was recorded with an energy range of 7670-7615 eV and an energy resolution of 0.25 eV. Next, two Co XAS spectra were measured with an energy range of 7702-7714 eV and an energy resolution of 0.2 eV. The sequence of XES and XAS (2x) was repeated for the nickel K-edge. For the nickel non-resonant XES spectrum the mono excitation was set at 8500 eV and an energy range of 7490-7465 eV and energy resolution of 0.25 eV were used. The energy range used for the Ni XAS spectra was 8328-8338 eV, recorded with an energy resolution of 0.2 eV.
To perform *in-situ* experiments, the catalyst sample was heated to elevated temperatures (60 °C, 95 °C, 140 °C, 200 °C, 270 °C and 450 °C) under dynamic H_2 flow through the reactor. When a certain temperature was reached, the reactor was kept at this temperature for approximately 1 hour. Then, before starting the measurement, the sample was cooled down to room temperature, while the reactor was kept under H_2 atmosphere. When the reactor reached room temperature the non-resonant XES measurement, followed by the two XAS measurements, were performed at the cobalt en nickel K-edge. In Figure 3.4a schematic representation of the *in-situ* experiment is shown.

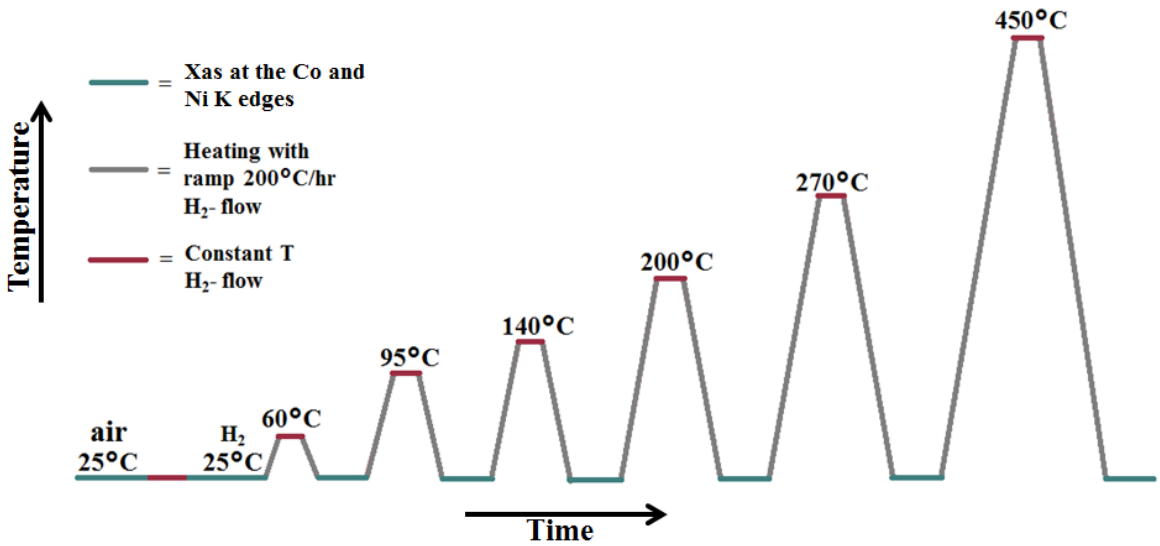

Figure 3.4: Overview of the *in-situ* XAS reduction experiment. To perform *in-situ* experiments the reactor catalyst sample was heated to several temperatures under dynamic H_2 flow through the reactor. The sample was allowed to react with H_2 with these conditions for 1 hour. XAS measurements for both the cobalt and nickel K-edge were performed at room temperature between each reaction step.

3.4.3 Scanning Transmission X-ray Microscopy

To study the presence and distribution of different species in oxide precursor samples, Scanning Transmission X-ray Microscopy (STXM) experiments were performed. Experiments were performed at the Canadian Light Source using spectromicroscopy(SM) beamline 10ID-1. The cobalt and molybdenum L_3-edges and aluminum K-edge were measured on the CoMoO2-seq sample, while for the CoNiMoO2-seq sample only the cobalt and nickel L_3-edges were measured. Energies corresponding to these edges are shown in Table 2.1. The samples were dispersed in iso-propanol and deposited on a siliconnitrate window (Figure 3.5a). The siliconnitrate window contains some areas with a window thickness of 10 nm, providing a better contrast for imaging. After evaporation of the isopropanol, a second window was aligned and glued on top of the siliconnitrate window (Figure 3.5b). The nanoreactor was placed inside the sample holder and was then screwed to the sample stage inside the STXM chamber (Figure 3.5c).

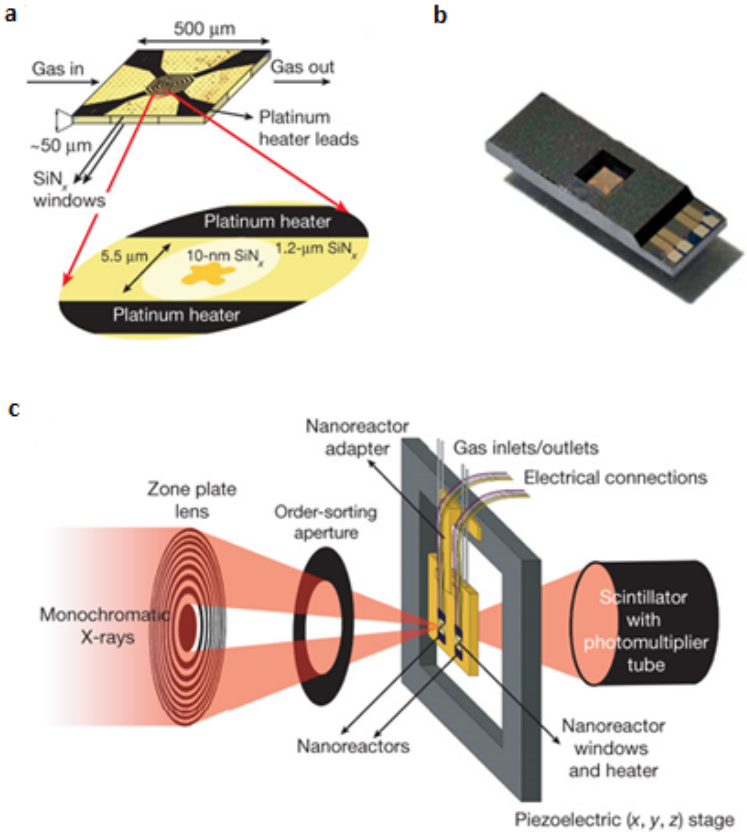

Figure 3.5: STXM set-up [44]. a) The sample was deposited on a silicon nitrate window, containing a platinum wire for heating. b) A second siliconnitrate window was glued on top of the first window, forming the nanoreactor. c) The nanoreactor was placed inside the sample holder and screwed to the sample stage inside the STXM chamber. The incoming X-ray beam was optimized by the zone plate and order-sorting aperture. Subsequently the sample was raster scanned in the x,y direction and transmitted X-rays were recorded.

3.4.4 Electron Energy Loss Spectroscopy

Extended STEM-EELS measurements were performed at the STEM group at the laboratoire de physique des solides, Université de Paris Sud. Measurements were done on a VG cold microscope. Samples were prepared by adding a drop of the catalyst dissolved in ethanol on a grid. Subsequently the grid was air-dried. A small amount of CoTiO reference sample was added to the oxide sample to facilitate the focusing on cobalt. For the sulfide sample, the sample preparation was done in a glovebox filled with N_2. Spectral images and some spectra were acquired. Additional STEM-EELS measurements were done on a NION USTEM 200. Sample preparation was similar to the preparation done for the VG cold microscope. To reduce contamination the samples were baked under vacuum for 10 hours at a temperature of 90 °C for the oxide and 80 °C for the sulfide. For the oxide samples, an accelerating voltage of 200kV was used. For measuring the sulfide samples, the accelerating voltage was reduced to 60kV. As samples were very sensitive to the electron beam, a fast mode was used with short acquisition time (<1ms) and a pixelsize of 1 nm.

4. Results and discussion

4.1 Standard catalyst characterization techniques

4.1.1 X-ray Diffraction

The X-ray powder diffraction patterns of the catalyst oxide samples are shown in Figure 4.1. The XRD pattern of the γ-alumina support is also shown. The peaks at diffraction angles of 38°, 44°, 46°, 54° and 80° verify the presence of γ-alumina support in all samples. Peaks around 27° and 31° indicate the presence of $CoMoO_4$ phases. These diffraction peaks are clearly visible for the CoMoO1-sim sample, while less pronounced for the CoMoO2-seq, CoNiMoO5-sim and CoNiMoO2-seg sample. This might indicate that the samples show less crystallinity or only small crystallites are present highly dispersed on the support. The NiMoO1-sim sample shows a peak at 31°, which is absent in the NiMoO2-seq sample and the rest of the samples. This diffraction peak could not be assigned to any of the possible species present.

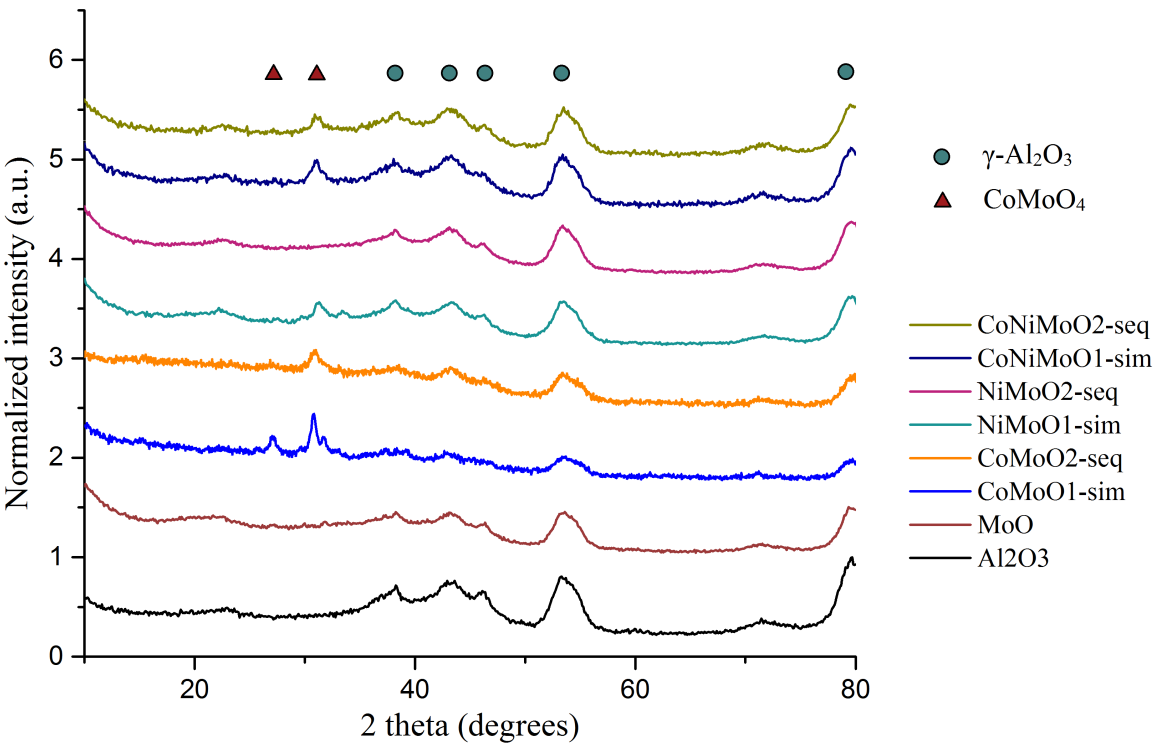

Figure 4.1: XRD diffractograms for all oxide precursor samples. Diffractograms were recorded using Co-Kα radiation with a wavelength of 1.79026 $\mathring{A}$.

4.1.2 Transmission Electron Microscopy

Representative TEM micrographs for the oxide and sulfide phase of each type of catalyst are shown in Figure 4.1.2. There were no noticable differences found in the morphology of samples prepared by different methods, or impregnated with the various promoters. Prior to the acquirement of the images no particles of molybdenum, cobalt or nickel were visible. However, the samples appeared to be very sensitive to electron beam damage as agglomerates

started to appear. This could indicate that prior to beam exposure the cobalt, nickel and molybdenum were highly dispersed on the support. EDX verified the presence of molybdenum and cobalt and/or nickel in all samples.

The sulfide catalysts all exhibit the well-know MoS_2 slab structure. No significant difference in slab length or dispersion of the slabs was found for the different sulfide samples. It should be noticed that the slabs are only visible with TEM if their edge is oriented towards the electron beam. Therefore it is likely that the number of slabs is higher than imaged with TEM. The presence of sulfur could not be verified by EDX as its emission signal overlaps with the emission signal for molybdenum.

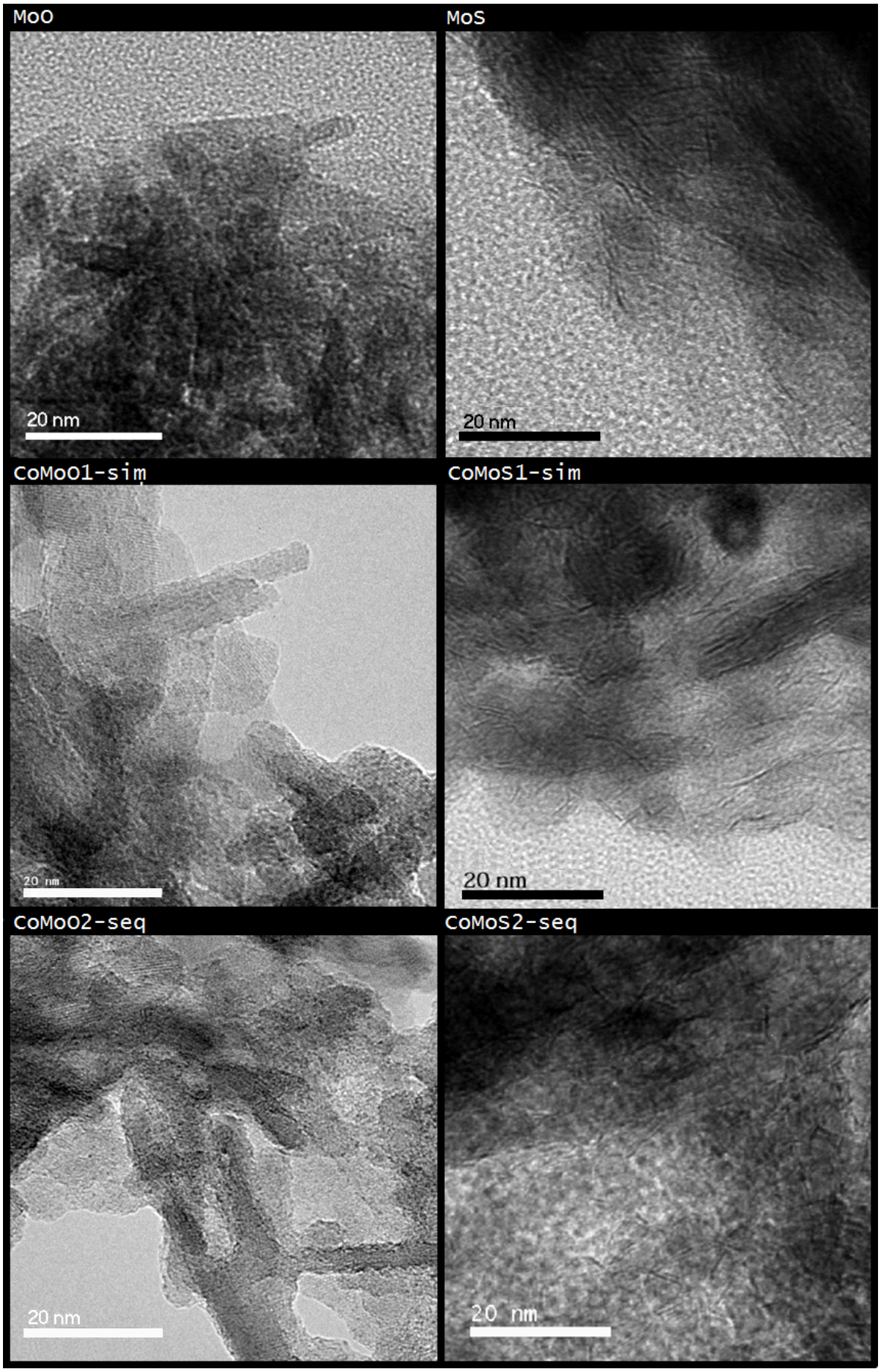
MoO
20 nm
MoS
20 nm
CoMoO1-sim
20 nm
CoMoS1-sim
20 nm
CoMoO2-seq
20 nm
CoMoS2-seq
20 nm

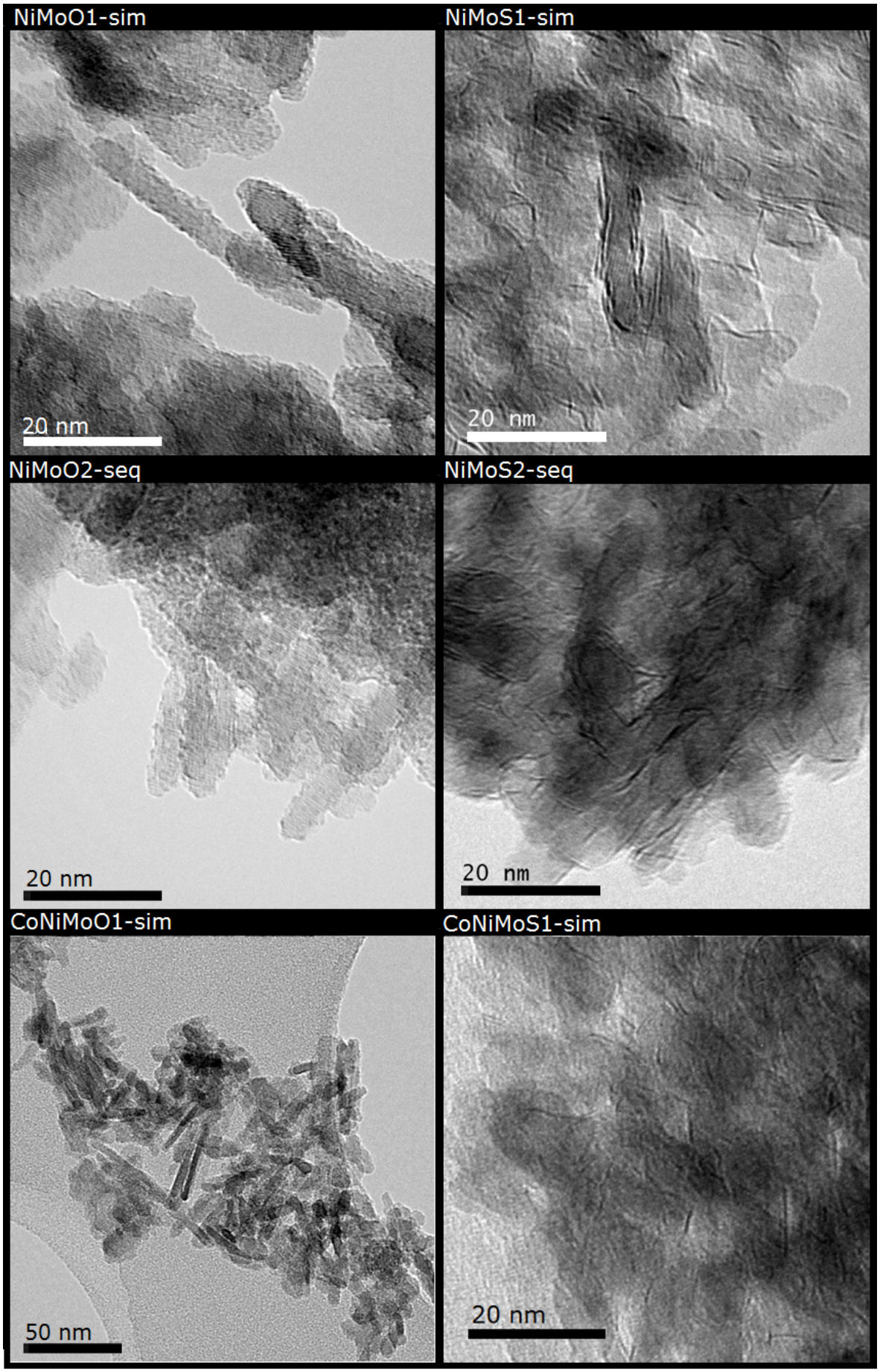
NiMoO1-sim
20 nm
NiMoS1-sim
20 nm
NiMoO2-seq
20 nm
NiMoS2-seq
20 nm
CoNiMoO1-sim
50 nm
CoNiMoS1-sim
20 nm

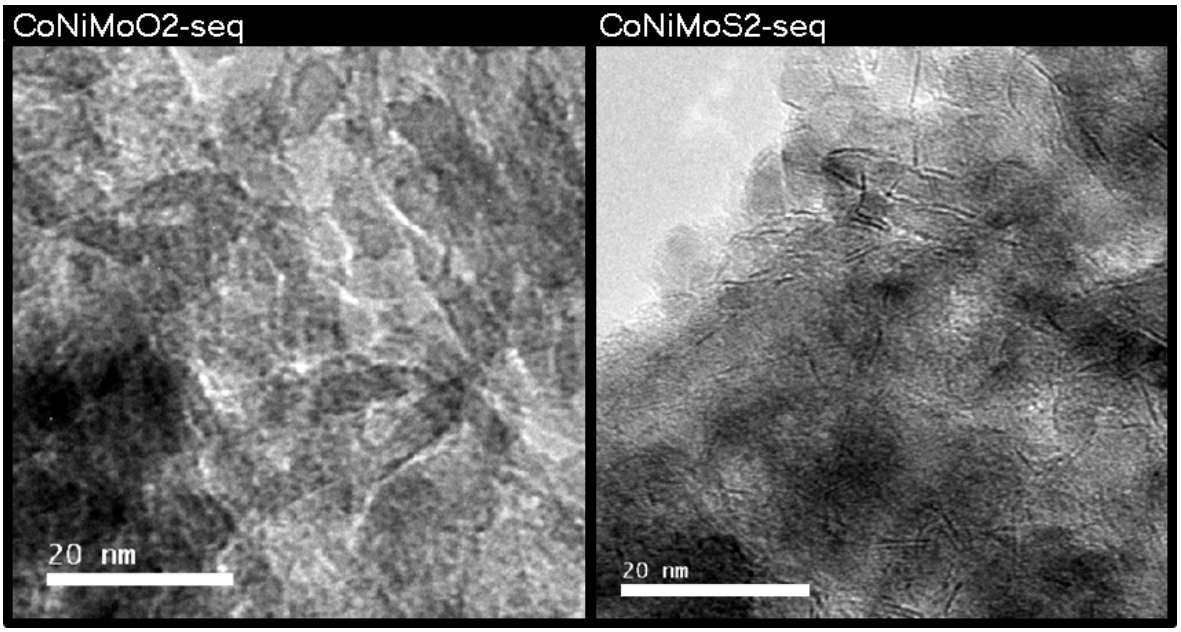

Figure 4.2: TEM images of the γ-alumina supported CoMo, NiMo and CoNiMo catalysts. Oxide catalyst precursors are shown on the right, while the corresponding sulfide catalysts are shown on the right.

4.2 Catalysis

The conversion of the catalyst samples in thiophene desulfurization was determined by a catalytic test performed at Ablemarle Catalyst BV.. Figure 4.3 shows the initial conversion and conversion after several thiophene pulses for all the synthesized catalysts. Since variation in molybdenum loading influences the HDS activity, the conversion is normalized for the molybdenum loading of the catalysts. All catalyst samples are active in the desulfurization of thiophene. The initial conversion of the unpromoted MoS catalyst is significantly lower than that of the promoted CoMoS, NiMoS and CoNiMoS catalysts. This verifies the promoting effect by cobalt and nickel. Catalysts promoted with the same elements, but prepared with a different impregnation sequence show differences in conversion. For the NiMoS catalyst, simultaneous impregnation results in higher initial conversion. A higher conversion for simultaneous impregnation is supported by Pawelec et al.(2008) [18,45]. It is suggested that in sequential impregnation the possibility of redissolving and redistribution is detrimental for catalyst activity. However, for the CoMoS and CoNiMoS catalysts sequential impregnation gives higher initial conversion. The lower conversion found for simultaneous impregnation could be explained by reaction of the metal precursors in the salt solution. During simultaneous impregnation, promoter and molybdenum salt precursors are dissolved in the same solution. As a consequence the formation of parasitic metal species is more likely to occur than for sequential impregnation. To determine if there is a significant trend between sequential impregnation and higher thiophene HDS conversion, reproducibility experiments are needed. The conversion of the double promoted CoNiMoS sample indicates that the double promotion decreases the conversion of the catalyst, when compared to the single promoted catalysts. This might be explained by the increased promoter to molybdenum ratio for double promoted catalysts. It is possible that due to the increased promoter:Mo ratio not all the cobalt or nickel atoms are positioned on the edges of the MoS_2 slabs. This can lead to an increase in the formation of cobalt and nickel bulk sulfide phases. As the active promoter

atoms are believed to be located on the edges of MoS_2, the formation of bulk sulfide phases will coincide with the lower conversion observed for double promotion. For most samples, the conversion slightly increases after stabilization of the catalyst. This could be explained by the fact that the activity of the catalyst is related to the dispersion and degree of sulfidation of the active phase [19]. During the addition of thiophene pulses, the degree of sulfidation and dispersion of the active phase can increase, resulting in higher conversions.

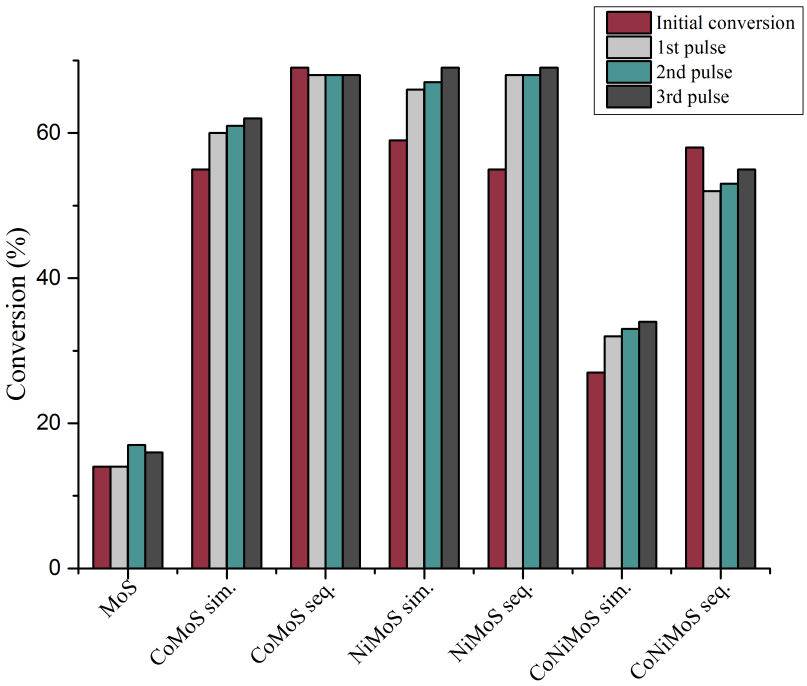

Figure 4.3: Conversion of different catalysts in thiophene HDS. Besides initial conversion, also conversion after stabilization is shown. Conversions are normalized for molybdenum loading.

4.3 Core level spectroscopy and microscopy

4.3.1 Sensitivity of cobalt and nickel towards oxidation

The sensitivity of cobalt and nickel towards oxidation was studied for a CoNiMoS3-sim sample in an *in-situ* X-ray absorption experiment. Figure 4.4 shows the cobalt K-edge XAS structures for various stages during the oxidation reaction. At first, a small shift of the edge towards higher energy is observed. The peak shift to higher energies corresponds to higher electron binding energies. This can be explained by a increase in the electrostatic interaction between the positive metal ion and negative electrons, caused by a decrease in shielding of charge by the absence of the extra electronic charge for higher oxidation states [46]. Therefore, a higher oxidation state corresponds to a higher electron binding energy and consequently the shift of the cobalt K-edge to higher energies verifies the oxidation of cobalt. At a temperature around 200°C the shift is significant and verifies the oxidation of most of the cobalt from 2+ to 3+. At 400 °C the spectral shape of the spectrum changes. This can be explained by the exchange of the ligands around the absorbing atom. During the oxidation the sulfur ligands are gradually exchanged for oxygen atoms. Besides the change in spectral shape, the ligand exchange also influences the pre-edge structure. The intensity of the pre-edge drastically decreases and at higher temperatures the peak also shows a small shift to lower

energies. The increase in intensity can be explained by a change in symmetry around the metal center. More intense pre-edge features are seen for noncentrosymmetric environments, due to increased mixing between the metal 4p states into the 3d orbitals. Consequently, additional character from the electric dipole allowed 1s4p transitions is added to the pre-edge feature [47]. To elucidate the trends seen for the pre-edge, the pre-edge structure of several cobalt oxide species was simulated using the software CTM4XAS (Figure 4.5). These calculations confirmed that during the oxidation of the sulfide sample, cobalt undergoes a symmetry change from tetrahedral to octahedral, as the decrease in cobalt pre-edge intensity already suggested. As mentioned before, the edge shift to higher binding energies verifies an oxidation of cobalt 2+ to cobalt 3+. However, from the calculations it was found that the cobalt 3+ O_h species would cause a pre-edge shift to slightly higher energies, contradicting with the pre-edge shift to lower energies observed in the experimental spectrum. As the cobalt 2+ O_h pre-edge is found at slighty lower energies, the calculated spectra suggest that, besides cobalt 3+ O_h, cobalt 2+ O_h is also present after oxidation. The presence of a mixture of cobalt 2+ O_h and 3+ O_h would lead to a lower pre-edge energy than observed for cobalt 2+ T_d. It is possible that cobalt undergoes a transition from cobalt 2+ T_d to cobalt 2+ O_h and that some of this cobalt 2+ O_h is further converted to cobalt 3+ O_h. Another possibility is that cobalt 2+ T_d changes directly to both cobalt 2+ O_h and cobalt 3+ O_h. In summary, from the edge and pre-edge analysis it is assumed that during the oxidation reaction, cobalt undergoes transitions from cobalt 2+ T_d species to a mixture of cobalt 2+ O_h species and cobalt 3+ O_h species.

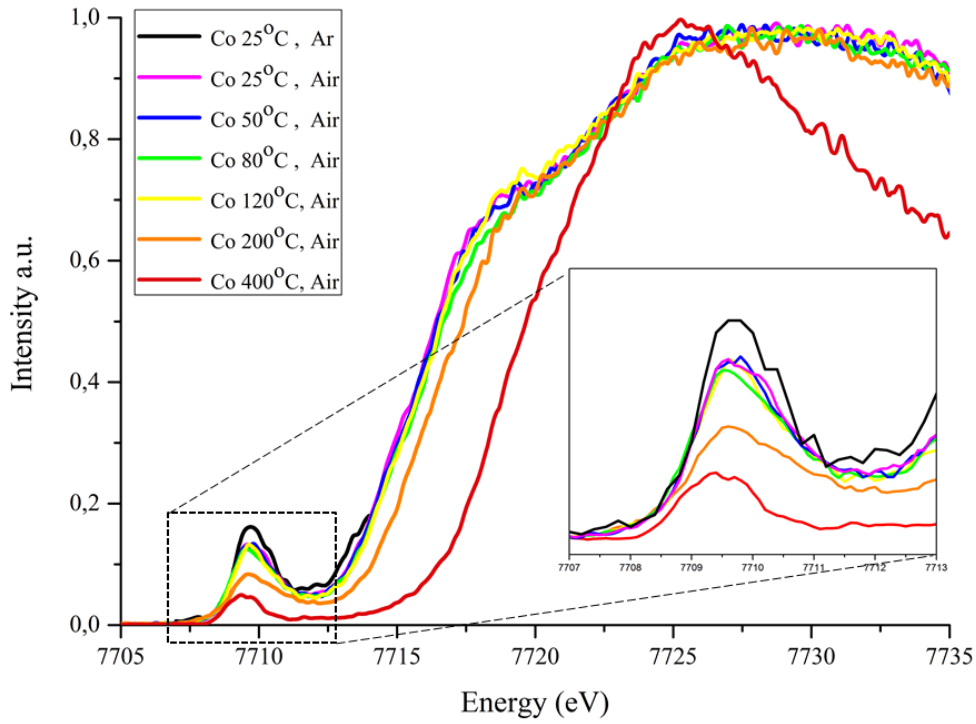

Figure 4.4: Cobalt K-edge X-ray absorption spectra during several stages of the oxidation experiment.

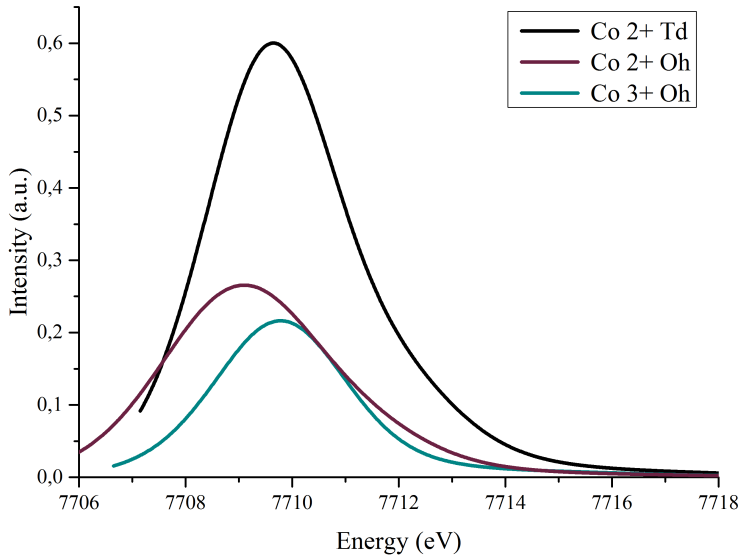

Figure 4.5: Cobalt K pre-edge region calculated by CTM4XAS for different symmetries and oxidation states.

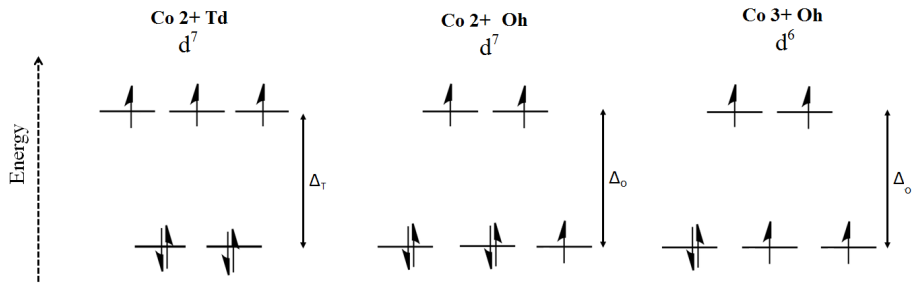

Figure 4.6: Spin systems for cobalt species. During the oxidation experiment a transition Co^{2+} $T_d \rightarrow Co^{2+}$ O_h and Co^{3+} O_h is observed.

Figure 4.7 shows the nickel K-edge spectra for the first two steps in the oxidation. Compared to the X-ray absorption spectra for cobalt, the quality of the nickel spectra is poor. This can be explained by the crystal lattice analyzer used for the measurements. The Si(311) crystal was optimized for the pre-edge region of the cobalt K-edge and consequently a smaller signal is measured for the nickel. Furthermore, by the use of a monochromator the energy is optimally calibrated for a narrow energy range, in this case the pre-edge. As a consequence, the signal-to-noise ratio is lower for energies outside the optimized pre-energy range. The nickel K-edge shows a shift towards higher energies, indicating the (partial) oxidation of nickel. The intensity of the nickel pre-edge shows a small decrease. This might be explained by a change in the coordination of the absorbing nickel atoms. During the oxidation of nickel sulfur ligands are exchanged by oxygen ligands. Consequently the geometry around the absorbing atom can slightly change, thereby influencing the mixing of 4p and 3d states. However, as the intensity decrease is not significant in this first step of the oxidation reaction it is unlikely that the symmetry is drastically altered in this first step. Additional measurements at higher temperatures are needed to elucidate if the symmetry of the nickel species

will change during oxidation at higher temperatures, as was the case for the cobalt species.

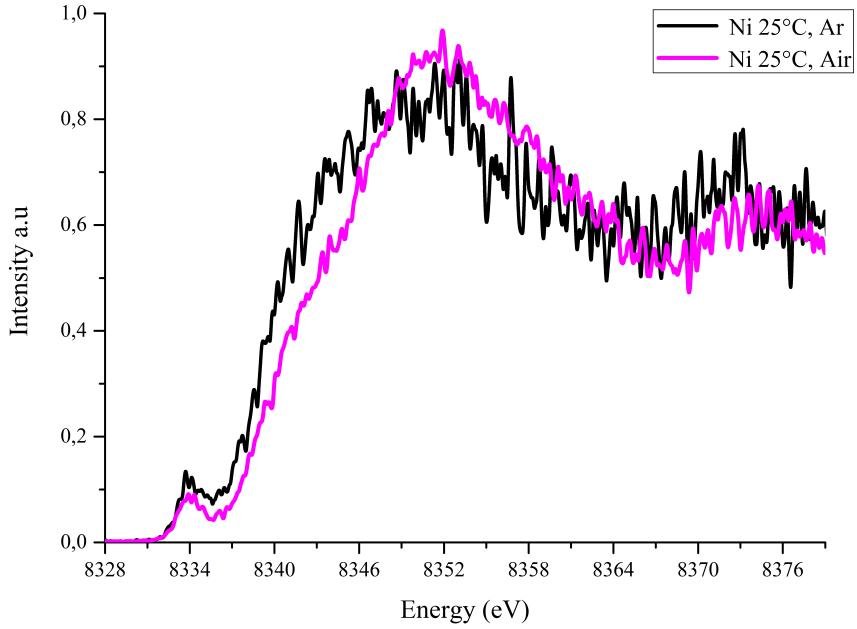

Figure 4.7: Nickel K-edge X-ray absorption spectra for the first two steps of the oxidation experiment.

4.3.2 Sensitivity of cobalt and nickel towards H_2 reduction

The sensitivity of cobalt and nickel towards H_2 reduction was studied for the CoNiMoO3-sim sample in an *in-situ* X-ray absorption experiment. Figure 4.8 summarizes the cobalt K-edge XAS structures for various stages of the reduction reaction. A shift of the cobalt K-edge (1s $\rightarrow$ 4p transitions) to lower energies is observed and indicates the reduction of cobalt. This shift already initiates by flowing H_2 at room temperature. However, the shift is not as significant as seen for the reduction reaction, suggesting that the valency of cobalt is not changed during the reduction and subsequently most of the cobalt species present after reduction will remain 2+.

The absorption features present in the cobalt pre-edge region correspond to the partially allowed quadrupole transitions from the 1s to the 3d shells. During the reduction experiment the intensity of the pre-edge peak increases, indicating a transition from octahedral symmetry to tetrahedral symmetry. Furthermore, in the experimental spectrum the pre-edge appears to shift to higher energies, which contradicts the trend seen for the edge. When looking back to simulated spectra in Figure 4.5, the change from a octahedral cobalt 2+ species to a tetrahedral cobalt 2+ species corresponds to a higher intensity of the cobalt pre-edge feature. Although the pre-edge shift to higher energies contradicts with the edge shift expected for reduction, the simulations indicate that a transition from a cobalt 2+ O_h species to cobalt 2+ T_d species correspond to a very small shift to higher energies. Consequently it is suggested that the small pre-edge shift is caused by the symmetry change from octahedral to tetrahedral. By combining the analyses of the edge and pre-edge it can be concluded that during reduction the symmetry of cobalt changes from octahedral to tetrahedral symmetry, while the valency remains 2+.

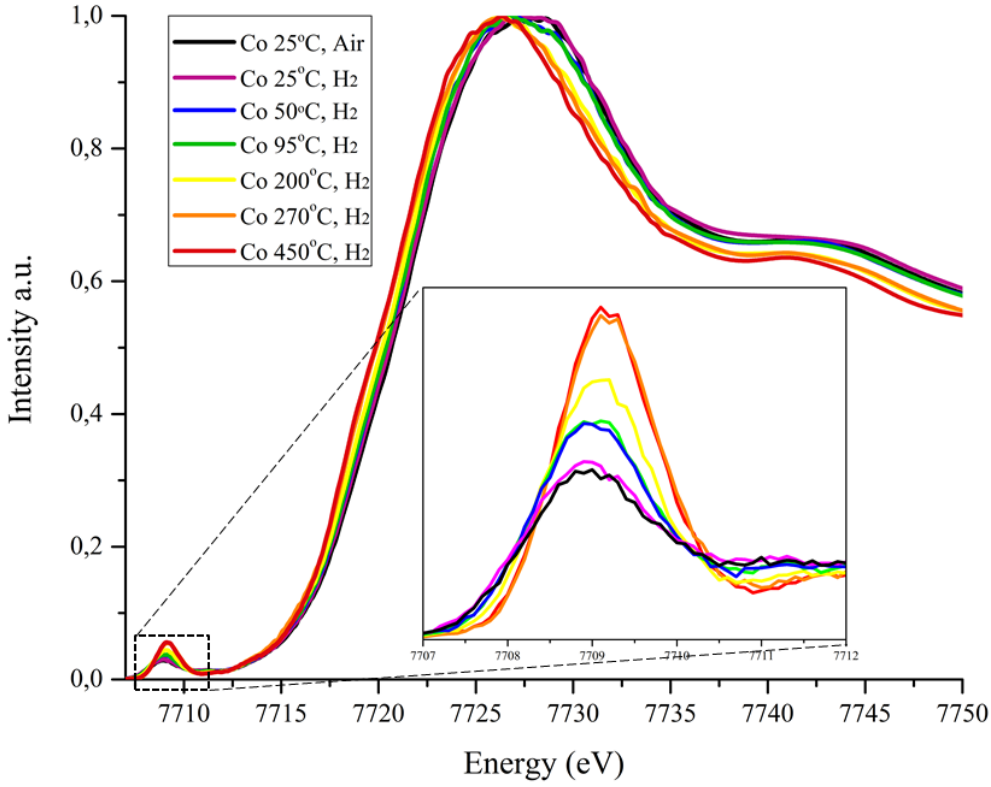

Figure 4.8: Cobalt K-edge X-ray absorption spectra recorded at several stages of H_2 reduction experiment.

Figure 4.9 shows the nickel K-edge XANES region for various stages during the reduction reaction. A small shift to lower energies can be seen for both the edge and the pre-edge. This indicates reduction of the nickel species. As only a small shift is seen, it might be that the nickel is not yet fully reduced. No change in intensity is seen for the pre-edge, suggesting that the symmetry of the nickel species remains the same during the during reduction experiment.

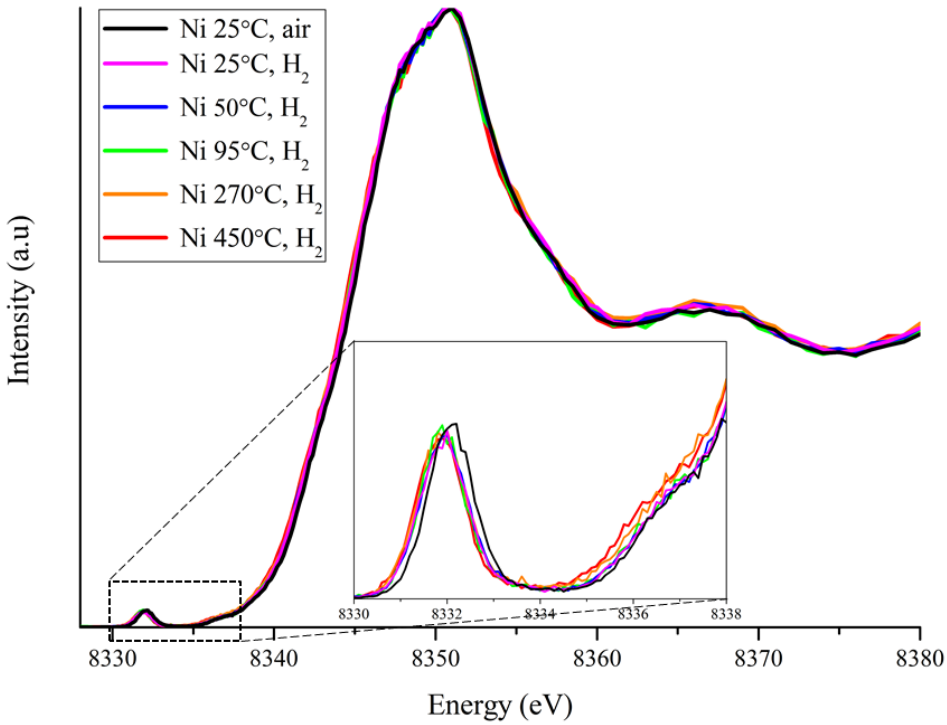

Figure 4.9: Nickel K-edge X-ray absorption spectra recorded at several stages of H_2 reduction experiment.

4.3.3 Study of the species present in HDS catalysts

Scanning Transmission X-ray Microscopy

Ex-situ STXM experiments were performed for the CoMoO2-seq and CoNiMoO2-seq samples. In Figure 4.10 the XANES spectra of the cobalt L_3-edge, the aluminum K-edge and the molybdenum L_3-edge are given. In Figure 4.10a the cobalt L_3-edge of the CoMoO-seq sample is plotted with two cobalt reference species, Co_3O_4 and CoO [48]. In Co_3O_4 cobalt has a mixed valence of 2+ and 3+, whereas the valence of cobalt in CoO is 2+. The splitting and positions of the peaks in the CoMoO spectrum correspond well with those found for the CoO reference spectrum. This strongly suggests the that the cobalt in CoMoO is present as CoO and thus as Co^{2+}. In Figure 4.10b the cobalt L_3-edge of CoMoO is compared to that of the CoNiMo sample. The edge pattern of both samples overlap, suggesting that CoO-like species are also present in the CoNiMoO sample. This corresponds with the results found in the *in-situ* reduction experiment, in which cobalt was present as cobalt 2+ Oh species in the CoNiMo oxide sample prior to the reduction reaction. In the CoNiMoO spectrum an additional shoulder is present around 781 eV. This might be due to the presence of nickel as this shoulder is absent in the CoMoO spectrum. Figure 4.10c compares the aluminum K-edge spectrum for the CoMoO sample with that of a γ-alumina reference spectrum [49]. The peak position and peak splitting of the CoMoO sample correspond well with that of the reference, verifying the presence of the γ-alumina support. Figure 4.10d shows a comparison between the experimental Mo L_3-edge of the CoMoO sample and a $MoO_3(Mo^{6+})$ reference spectrum [50]. The position of the peak corresponds well. Due to the low resolution of the STXM beamline, spectral features could not be identified for the Mo L_3-edge.

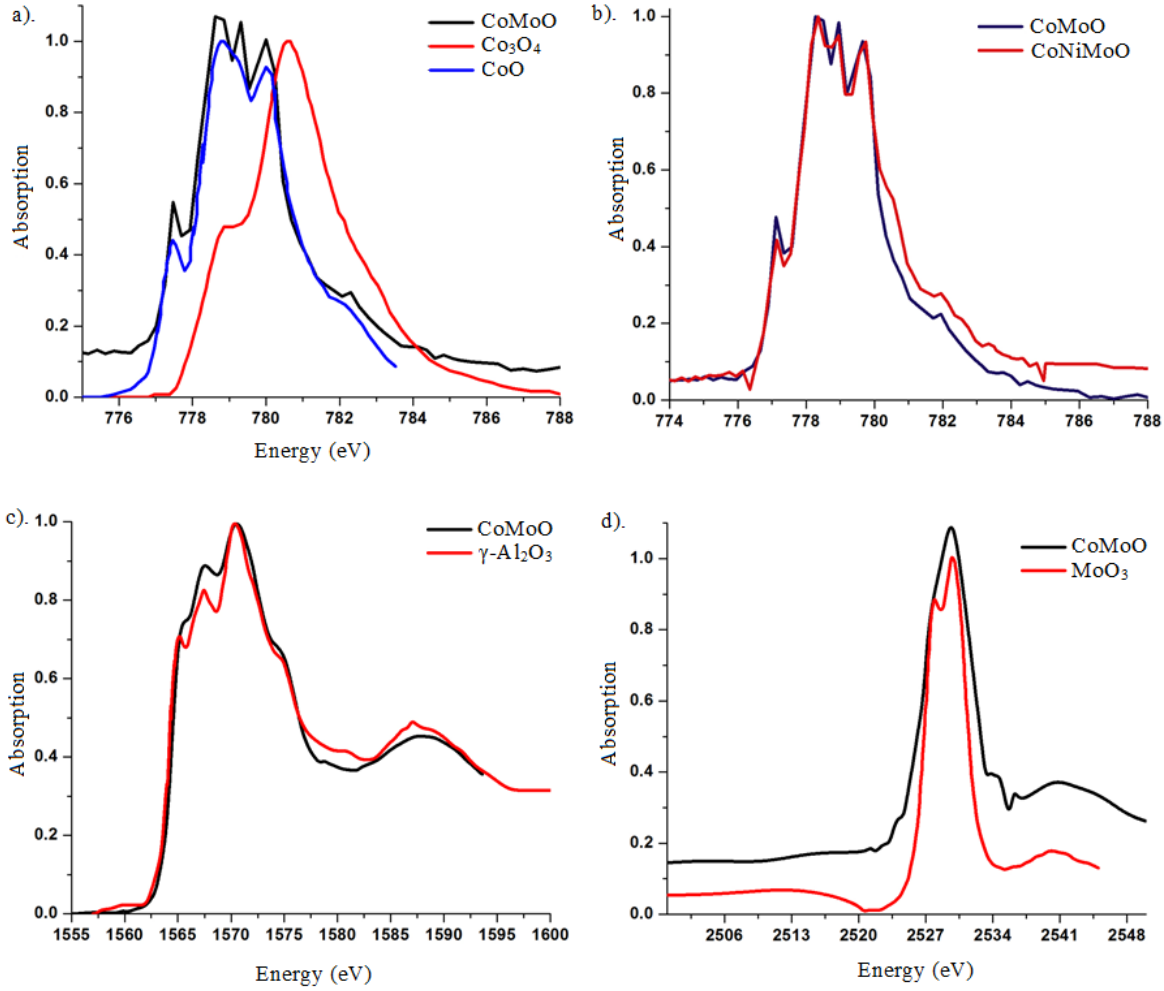

Figure 4.10: XANES structures for the CoMoO and CoNiMoO samples. a) The Cobalt L_3-edge of the CoMoO sample plotted together with two cobalt reference species (Co_3O_4 and CoO). b) The cobalt L_3-edges of the CoMoO and CoNiMoO samples. c) The aluminum K-edge overlaps with a γ-alumina reference spectrum. d) The molybdenum L_3-edge overlaps with a MoO_3 reference spectrum.

From the raster scanned XANES structures, a 2D spectral elemental map was generated. In order to obtain the elemental maps the pre-edge image is substracted from the image taken at the respective edge. The elemental maps indicate the distribution of the measured elements. For the CoMoO sample the aluminum, cobalt and molybdenum elemental maps are shown in Figure 4.11a,b and c, respectively. The aluminum K-edge map shows the morphology of the support particle. As a consequence of low photon flux at the Mo L_3-edge, a low quality spectral elemental map was obtained for molybdenum. From the cobalt and molybdenum maps it can be seen that the cobalt and molybdenum are not well dispersed.

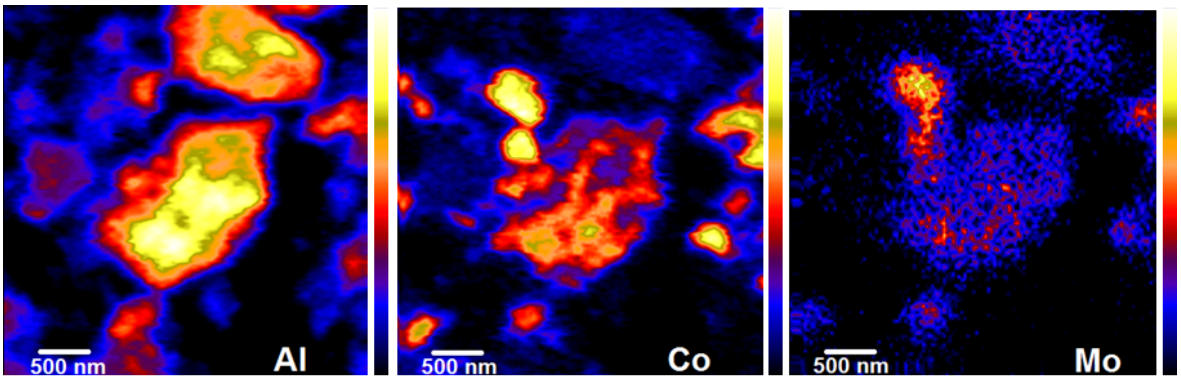

Figure 4.11: Spectral elemental maps for the Al K-edge, Co L_3-edge and Mo L_3-edge for the CoMoO sample.

Figure 4.12 gives the spectral elemental maps of the CoNiMoO-seq sample. For this sample only the cobalt and nickel edges were measured. By comparing the cobalt and nickel maps one can see that the distribution of cobalt is similar to that of nickel. However, also some areas are present where either cobalt or nickel is more abundant.

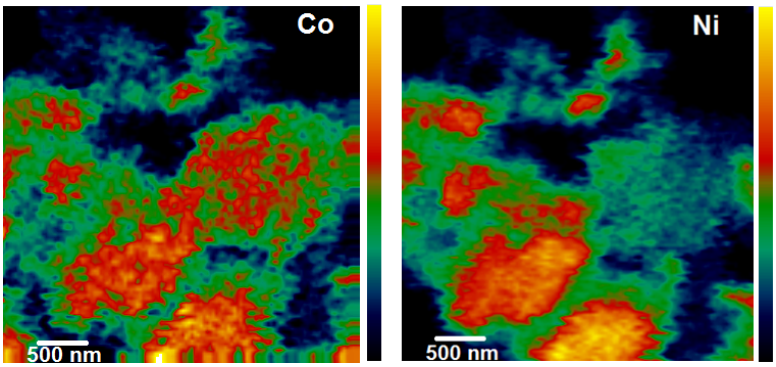

Figure 4.12: Spectral elemental maps for the Co and Ni L_3-edge of the CoNiMoO sample.

4.3.4 Scanning Transmission Electron Microscopy - Electron Energy Loss Spectroscopy

The first session of STEM-EELS measurements were performed using a VG cold microscope. For the CoNiMoO2-seq sample elemental maps were obtained from several spots of the sample. Unfortunately the signal to noise ratio was very low. Furthermore the weight loading of molybdenum and especially cobalt and nickel was low, which made it difficult to focus the electron beam. As a result the elemental maps have a poor quality and no relevant information could be extracted from the obtained low quality spectra. Figure 4.13 shows the elemental maps for molybdenum, cobalt, nickel and oxygen for two different location on the CoNiMoO2-seq sample. The oxygen map gives information about the morphology of the γ-alumina support, however oxygen is also present in the metal oxide species. Cobalt and nickel distributions were compared at several locations on the catalyst particles. Both elements showed exactly the same distribution at almost all pixels of the elemental maps. As it is unlikely that the cobalt and nickel have exactly the same distribution on multiple locations on the particle, this might be an artifact of the denoizing procedure. Furthermore the sample CoNiMoS2-seq was studied. The sulfide sample was exposed to air during sample preparation stage and during introduction into the microscope chamber. Therefore, the probability of

partial oxidation of the sulfides exists. Besides the oxidation, the sample was very sensitive to the electron beam. Although a CoTiO reference was added to facilitate focusing on cobalt, it was difficult to obtain a good focus. Consequently some poor quality images were acquired for the sulfide sample, but the signal to noise ratio was too low to obtain useful spectra and determine the oxidation state of the elements. Several different sample locations were studied, but no typical MoS_2 slabs could be identified. However, previous acquired TEM images did show the MoS_2 slabs. This suggest the oxidation and beam damage modified the structure and consequently the results obtained in this measurements are not representative for the active HDS catalyst.

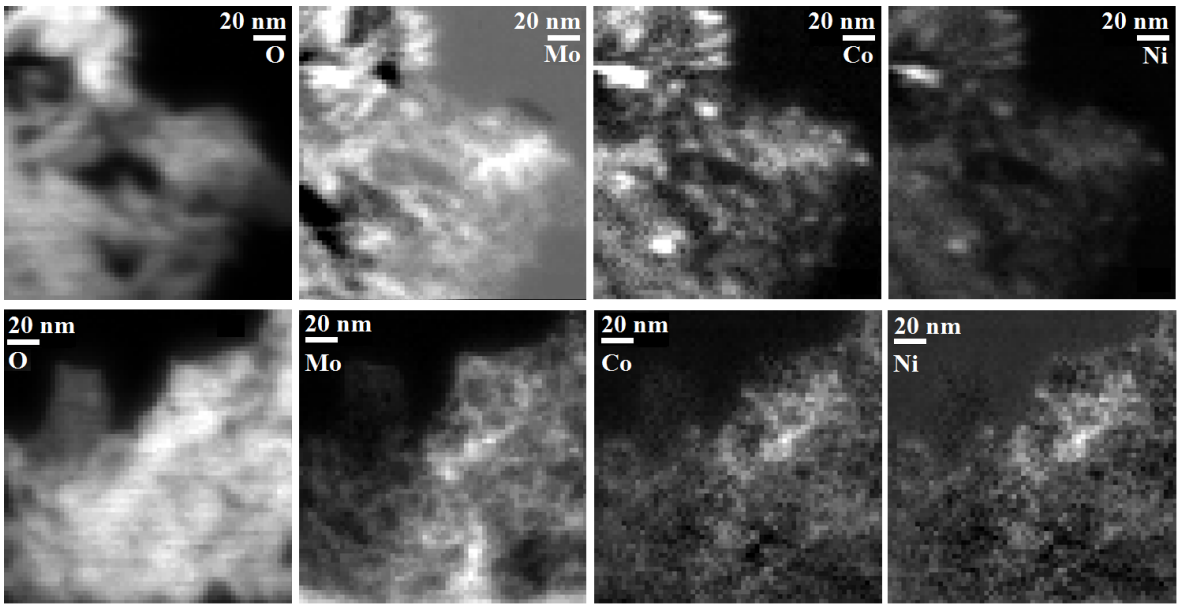

Figure 4.13: Poor quality elemental maps acquired with STEM-EELS (CoNiMoO2-seq.). The top and bottom series represent different locations on the sample. The molybdenum distribution roughly corresponds to the support particle. The cobalt and nickel maps show some differences in distribution compared to the molybdenum. However, the cobalt and nickel maps show exactly the same distribution. This might be an artifact of the denoizing procedure.

For the second STEM-EELS session measurements were performed using a NION USTEM 200 microscope. First, the CoNiMoO3-sim sample was studied. A fast mode was applied to minimize beam damage to the sensitive sample. During image acquirement first no molybdenum, cobalt or nickel particles were visible. However, after exposure of the sample to the electron beam small particles (∼1nm) were formed. This could indicate that the metals are present on the sample and might be homogeneously distributed prior to beam damage. Due to a low signal to noise ratio and low energy resolution it was not possible to determine the oxidation state of the different metals from energy loss spectra. In addition the CoNiMoS3-sim sample was also studied. For this sample the sample preparation was performed in a glovebox, minimizing the exposure to air. Again a fast mode was used to minimize the effect of beam damage. MoS_2 slabs were present in mono- and multilayers (Figure 4.14. Unfortunately the slabs were immediately destroyed by the beam.

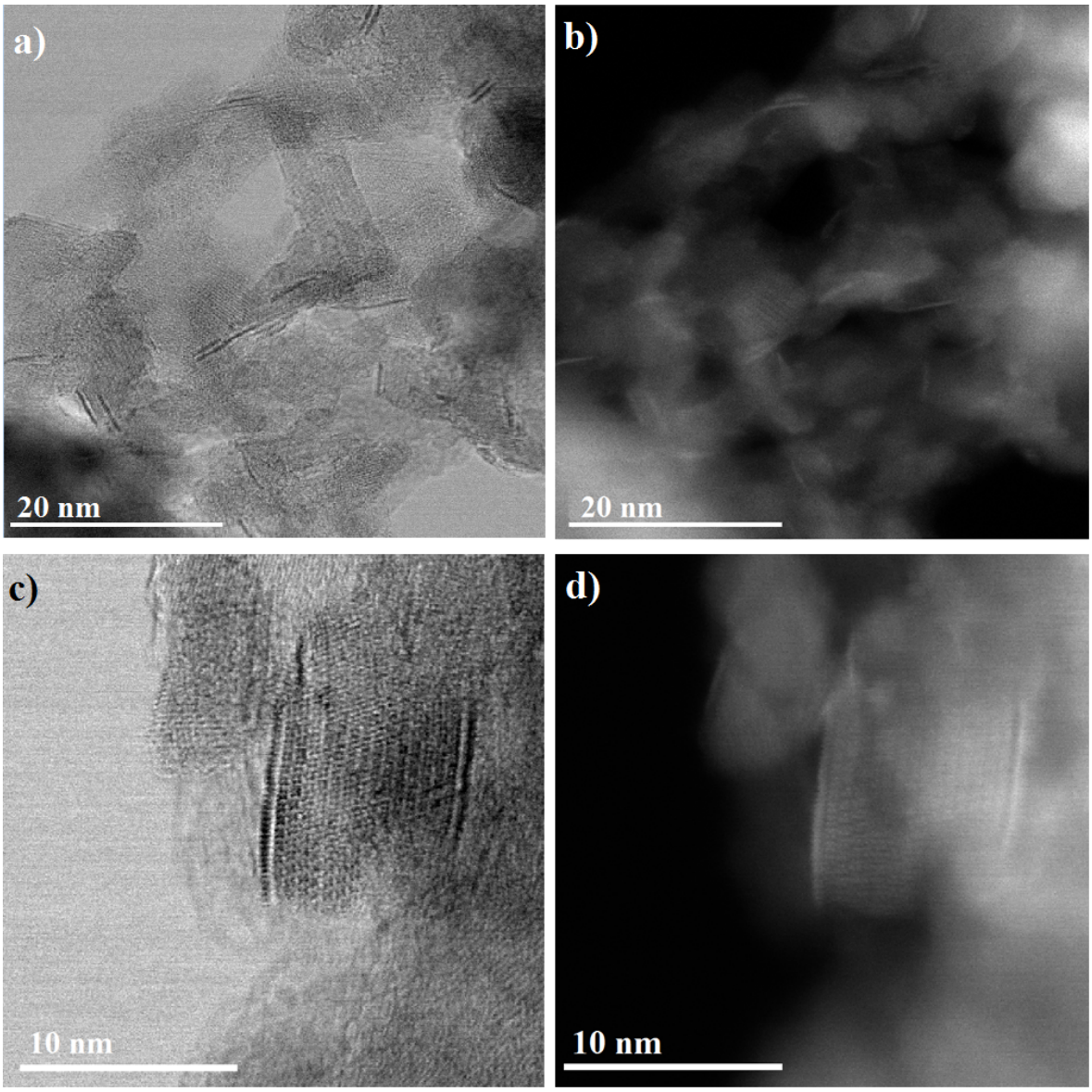

Figure 4.14: High resolution STEM images of the CoNiMoO3-sim sample recorded in bright (a,c) and dark field (b,d) mode. MoS_2 slabs are visible in mono- and multilayer structures.

5. Conclusion

γ-alumina supported MoS, CoMoS, NiMoS and CoNiMoS HDS catalysts were prepared by incipient wetness impregnation, followed by drying, calcination and sulfidation processes. The effect of different impregnation methods on catalysts morphology and activity was studied by comparing sequential and simultaneous impregnation of molybdenum and promoters. By the use of XRD, TEM and catalytic tests, no difference in morphology of the active phase or catalytic activity was found for simultaneous and sequential impregnated catalysts. Furthermore, the differences between promoters and possible synergistic effects of double promotion were studied. By the use of XRD and TEM, no significant differences in morphology or species present were found between different promoted catalysts. Catalytic tests in thiophene desulfurization verified the promoting effect by cobalt and nickel, since their addition yielded a higher conversion compared to the unpromoted sample. No significant differences in conversion were found for cobalt and nickel promoted catalysts or sequential and simultaneous impregnated catalysts. However, the double promoted CoNiMoS catalysts showed a lower conversion rate compared with the single promoted CoMoS and NiMoS catalysts, suggesting the absence of a synergistic effect for double promotion. It is suggested that the lower conversion is caused by the different ratio between the promoter and molybdenum, resulting in higher concentrations of bulk sulfide phases.

The sensitivity of cobalt and nickel towards oxidation was studied for a CoNiMo sulfide using *in-situ* X-ray absorption spectroscopy. For cobalt the K-edge shifted to higher energies. At temperatures above 200 °C, a drastic increase in edge energy together with a change in spectral shape suggests the oxidation of cobalt 2+ to 3+ and the exchange of sulfur ligands for oxygen ligands. The decrease in pre-edge intensity can be explained a transition from tetrahedral symmetry to octahedral symmetry, as simulated by CTM4XAS calculations. Combining the information obtained from the edge and pre-edge suggests that during oxidation cobalt undergoes a transition from cobalt 2+ tetrahedral system to a mixture of cobalt 2+ octahedral and cobalt 3+ octahedral species (Co^{2+} $T_d \rightarrow Co^{2+}$ O_h and Co^{3+} O_h). For nickel K-edge showed a shift to higher energies, suggesting gradual oxidation of the nickel species.

Furthermore, the sensitivity of cobalt and nickel species towards H_2 reduction was studied for a CoNiMo oxide by *in-situ* X-ray absorption spectroscopy. An edge shift to lower energies was observed for the cobalt K-edge, corresponding to a reduction of the cobalt. The pre-edge showed an increase in intensity and shift to higher energies. It was found that the symmetry of the cobalt oxide species changes from octahedral to tetrahedral symmetry during the reduction reaction (Co^{2+} $O_h \rightarrow Co^{2+}$ T_d). For the nickel K-edge and pre-edge, a shift to lower energies was observed, thereby confirming reduction. It was concluded that the coordination around nickel remained the same during the reduction reaction, as no significant intensity change was observed in the pre-edge region.

Scanning Transmission X-ray Microscopy was used to study presence and distribution of species present on the catalyst particle. From the XANES region is was found that cobalt is present as CoO in both CoMoO2-seq and CoNiMoO2-seq. Molybdenum was found as MoO_3 in CoMoO2-seq. Spectral elemental maps for cobalt, nickel, molybdenum and aluminum showed that the distribution of the different species was not very homogeneous. However, to obtain more representative results, more particles of the sample should be analyzed.

6. Future work

The sulfidation process, in which the catalyst oxide precursor is converted into the active sulfide calatyst, is an important process in the HDS catalyst synthesis. It was suggested that different sulfiding temperatures lead to different CoMoS phases [51,52]. At low temperature a CoMoS I phase is formed with strong electronic interaction with the support, whereas at high temperatures the more active CoMoS II phase is formed with a weak electronic interaction with the support. Furthermore, it was found that the heating rate is a fundamental parameter in the sulfidation [53]. A lower heating rate results in a better dispersion and sulfidation of the active phase, leading to a higher catalytic activity. The original aim of this project was to study the sulfidation procedure using *in-situ* Scanning Transmission X-ray Microscopy (STXM) and Resonant Inelastic X-ray Scattering (RIXS) to elucidate the local chemical composition during the sulfidation reaction. Due to issues with the radiation facility and safety issues with H_2S gas, used for the sulfidation procedure, it was impossible to perform any *in-situ* sulfidation experiments. Since the HDS activity is related to dispersion and degree of sulfidation of the active phase, it would be interesting to continue with the study of the presence and distribution of different species prior, during and after the sulfidation process. This might lead to a better understanding of the sulfidation procedure and consequently to new insights for improvements of the procedure.

Furthermore, it would be very interesting to study an *in-situ* HDS reaction using X-ray absorption spectroscopy and microscopy. In this way the oxidation state, coordination and distribution of various species can be studied during catalytic reaction. This can give new insights in the catalytic behavior, which can help to improve the catalyst.

References

[1] U.S. Energy Information Administration, International Energy Outlook: World Petroleum and Other Liquid Fuels (2014). Available: http://www.eia.gov/forecasts/ieo/pdf/0484 (2014).pdf. Last accessed 14th October 2014.

[2] I. Choerkendorff, J.W. Niemantsverdriet. Concepts of Modern Catalysis en Kinetics, Wiley-VHC Verlag GmbH & Co. KGaA, Weinheim, Germany. p353-364 (2003).

[3] A. Aguirre-Gutiérrez et al. J. Mol. Catal. A. 346, p.12-19 (2011).

[4] S. Eijsbouts et al. Cat. Today. 130, p.361-373 (2008).

[5] Vimal Chandra Srivastava, RSC Advances. 2, p.759-783 (2012).

[6] J.N. Diaz de Leon et al. J. Mol. Catal. A. 323, p.1-6 (2010).

[7] H.A. El Masry. Appl. Catal. 16, p301-313 (1985).

[8] M.P. Elsner. Cat. Today. 78-80, p487-494 (2003).

[9] F. Schuth et al. Handbook of Porous Solids. Vol. 3 Wiley-VHC Verlag GmbH & Co. KGaA, Weinheim, Germany. p.1652-1663 (2002).

[10] M. Breysse et al. Cat. Today. 86, p5-16 (2003).

[11] H. Tops*o*e, B.S. Clausen. Appl. Catal. 25, p.273-293 (1986).

[12] R. Javadli, A. de Klerk. Appl. Petrochem. Res. 1, p3-19 (2012).

[13] F. Bataille et al. J. of Cat. 191, p409-422 (2000).

[14] J. Kibsgaard et al. J. of Cat. 272, p195-203 (2010).

[15] H. Tops*o*e. J. of Cat. 68, p433-452 (1980).

[16] P.G. Moses et al. Catal. Lett. 144, p1425-1432 (2014).

[17] Eijsbouts, S. Hydrotreating Catalysts, in Synthesis of Solid Catalysts (ed K. P. de Jong), Wiley-VCH Verlag GmbH & Co. KGaA, Weinheim, Germany. p314-315 (2009).

[18] B. Pawelec et al. Appl. Surface Science. 254 p.4092-4102 (2008).

[19] Eijsbouts, S. Hydrotreating Catalysts, in Synthesis of Solid Catalysts (ed K. P. de Jong), Wiley-VCH Verlag GmbH & Co. KGaA, Weinheim, Germany. p318-323 (2009).

[20] J.A. Rodriguez et al. J. Phys. Chem. B. 103, p770-781 (1999).

[21] J.A. Rodriguez et al. J. Phys. Chem. B. 102, p1347-1355 (1998).

[22] J. Zou and G.L. Schrader. J. of Cat. 161, p667-686 (1996).

[23] J. J. Krummenacher. J. of Cat. 215, p332-343 (2003).

[24] P.E. de Jongh. Physisorption: as characterisation technique for porous and non-porous materials, Utrecht University, Lecture slides of the course Adsorption, kinetics and Catalysis (2014).

[25] J.W. Niemantsverdriet. Diffraction and extended x-ray absorption fine structure (EXAFS). In: Spectroscopy in catalysis, an introduction. 3rd ed., Weinheim: WILEY-VCH Verlag GmbH & Co. KGaA, p148-152 (2007).

[26] J.W. Niemantsverdriet. Microscopy and Imaging. In: Spectroscopy in catalysis, an introduction. 3rd ed., Weinheim: WILEY-VCH Verlag GmbH & Co. KGaA, p179-184 (2007).

[27] J.W. Niemantsverdriet. Elemental analysis in the Electron Microscope. In: Spectroscopy in catalysis, an introduction. 3rd ed., Weinheim: WILEY-VCH Verlag GmbH & Co. KGaA, p190-193 (2007).

[28] F.M.F. de Groot. X-ray absorption spectroscopy and microscopy. Utrecht University, Lecture slides of the course Advanced spectroscopy of nanomaterials (2014).

[29] F.M.F. de Groot and A. Kotani. Core Level Spectroscopy of Solids. Taylor & Francis Group LLC. p11-28.(2008).

[30] Canadian Light Source, How a synchrotron works (2014). Avialable: http://www.lightsource.ca/education/images/whatis/whatis-a-overview-of-synchrotron_light.jpg. Last accessed 31st October 2014.

[31] Diamond Light Source, How Diamond works (2014). Available: http://www.diamond.ac.uk/Public/How-Diamond-Works.html. Last accessed 29th January 2015.

[32] F.M.F. de Groot. Coord. Chem. Rev. 249, p31-63 (2005).

[33] G. Henderson et al. Reviews in Mineralogy & Geochemistry. 78, p.75-138 (2014).

[34] S. R. Bare. XANES Measurements and Interpretation. EXAFS Data Collection and Analysis Course, NSLS (2003). Available: http://chemistry.st-and.ac.uk/staff/gh/teaching/CH5711/Further%20reading/xanes.pdf. Last accessed 30th October 2014.

[35] F. Hippert et al. Neutron and X-ray spectroscopy. Springer. p4-10.(2006).

[36] F.M.F. de Groot et al. J. Phys. Chem., 109 , p.20751-20762.(2005).

[37] X-ray Data Booklet, LBNL, Berkeley (2009).

[38] Paul Scherrer Institut, X-ray probes of chemical dynamics. Available: http://www.psi.ch/swissfel/x-ray-probes-of-chemical-dynamics. Last accessed 29th January 2015.

[39] Canadian Light Source, Soft X-Ray Spectromicroscopy (2014). Available: http://www.lightsource.ca/education/whatis.php. Last accessed 29th January 2015.

[40] R.F. Egerton. Rep. Prog. Phys. 72. 25pp (2008).

[41] G. Berhault. J. of Cat. 198, p9-19 (2001).

[42] N.D. Browning. Micron 28 p333-348 (1997).

[43] E. Stavitski and F. de Groot. Micron 41, p687-694 (2010).

[44] E. de Smit et al. Nature. 456, p222-225 (2008).

[45] R. Nava et al. Appl. Catal. A. 321, p58-70 (2007).

[46] D. Joseph et al. Nucl. Instrum. Methods Phys. Res. Sect. B. 274, p126-128 (2012).

[47] T. E. Westre et al. J. Am. Chem. Soc. 119, p6297-6314 (1997).

[48] D. Bazin et al. Appl. Catal. A. 242, p179-186 (2003).

[49] C.S. Doyle et al. J. Synchrotron Rad. 6, p621-623 (1999).

[50] H. Aritani et al. Appl. Surf. Sci. 180, p261-269 (2001).

[51] R. Candia. Bull. Soc. Chim. Belg. 93, p763-773 (1984).

[52] H. Shimada. Cat. Today. 86, p17-29 (2003).

[53] Villarreal, A. et al. Cat. Today. 2014 (In press).